

THE MASS SPECTRUM OF THE FIRST STARS

HAJIME SUSA¹, KENJI HASEGAWA², AND NOZOMU TOMINAGA^{1,3}

Department of Physics, Konan University, Okamoto, Kobe, Japan¹
Center for Computational Science, University of Tsukuba, Japan² and
Kavli Institute for the Physics and Mathematics of the Universe (WPI),
The University of Tokyo, 5-1-5 Kashiwanoha, Kashiwa, Chiba 277-8583, Japan³
Draft version August 1, 2018

ABSTRACT

We perform cosmological hydrodynamics simulations with non-equilibrium primordial chemistry to obtain 59 minihalos that host first stars. The obtained minihalos are used as initial conditions of local three dimensional radiation hydrodynamics simulations to investigate the formation of the first stars. We find two-thirds of the minihalos host multiple stars, while the rest of them have single stars. The mass of the stars found in our simulations are in the range of $1M_{\odot} \lesssim M \lesssim 300M_{\odot}$, peaking at several $\times 10M_{\odot}$. Most of the very massive stars of $\gtrsim 140M_{\odot}$ are born as single stars, although not all of the single stars are very massive. We also find a few stars of $\lesssim 1M_{\odot}$ that are kicked by the gravitational three body interactions to the position distant from the center of mass. The frequency that a star forming minihalo contains a binary system is $\sim 50\%$. We also investigate the abundance pattern of the stellar remnants by summing up the contributions from the first stars in the simulations. Consequently, the pattern is compatible with that of the low metallicity Damped Lyman- α systems or the Extremely Metal Poor (EMP) stars, if the mass spectrum obtained in our experiment is shifted to the low mass side by 0.2 dex. If we consider the case that an EMP star is born in the remnant of the individual minihalo without mixing with others, the chemical signature of the pair instability supernova is more prominent, because most of them are born as single stars.

Subject headings: early Universe—radiative transfer—first stars—metal poor stars

1. INTRODUCTION

Formation of the first stars is one of the central objectives of modern cosmology, which has been intensively investigated from the end of the last century. We now have the standard model that the first stars form at the redshift of $z \gtrsim 20$, in the minihalos which are as massive as $10^5 - 10^6 M_{\odot}$ (Haiman et al. 1996; Tegmark et al. 1997; Nishi & Susa 1999; Fuller & Couchman 2000; Abel et al. 2002; Bromm et al. 2002; Yoshida et al. 2003). In such minihalos, the gas temperature cannot rise up to 10^4 K by gravitational contraction, because the virial temperature is low. Thus, the only available coolant in the gas is H_2 molecules, since H Ly α cooling is not activated and no heavy elements exist at that very early Universe.

H_2 molecule is an inefficient coolant, because it is a homonuclear diatomic molecule. Hence, the gas temperature of the primordial gas tend to be higher than that of the interstellar gas, in which more efficient coolant such as metals and dusts exist. In fact, the gravitationally contracting gas temperature in the primordial minihalo for $\lesssim 10^8 \text{cm}^{-3}$ is $200\text{K} \sim 10^3\text{K}$, which is higher than the temperature of the interstellar gas by roughly two orders of magnitude. The Jeans mass of the dense core of $\sim 10^4 \text{cm}^{-3}$ in the minihalo is $10^2 - 10^3 M_{\odot}$, which is much larger than the present-day counterpart ($\sim 1M_{\odot}$). In addition, the mass accretion rate onto the central star is proportional to $T^{3/2}$, that is also very high in primordial case. Based upon these theoretical evidences, the typical mass of the first stars is once considered to be very high ($\gtrsim 100M_{\odot}$).

On the other hand, recent advance in the studies on the

mass accretion phase of the first star formation revealed that the mass of the first stars could be smaller than expected before (Clark et al. 2008; Smith et al. 2011). The highest spatial resolution achieved among these studies is less than 1AU, which enables them to resolve the fragmentation of the gas disk that form in the very vicinity of the primary first star. They found that a “cluster” of lower mass stars could form rather than a single very massive star (Clark et al. 2011a,b; Greif et al. 2011, 2012; Machida & Doi 2013). In addition, statistical studies have revealed that there are various cases of multiplicity in a minihalo, depending on the properties of the collapsing cloud (Stacy & Bromm 2013).

On the other hand, the final mass of the stars are not fixed by the first several thousand years after the formation of the primary star. It will take several tens of thousand years until the stars settle onto the main sequence stars, which is hardly possible to be followed by very high resolution studies. In addition, ultraviolet radiative feedback from the protostar comes into play after the mass of the protostar grows to $\sim 20M_{\odot}$. Thus, we have to take into account the radiative feedback properly.

The effects of ultraviolet radiation from the protostars on the mass accretion flow were first investigated by Omukai & Palla (2001). They constructed a one dimensional spherical steady model of accreting protostar, and they found the radiation cannot stop the mass accretion onto the protostar if typical mass accretion rate inferred by the cosmological simulation is adopted (Omukai & Palla 2003). Tan & McKee (2004) have constructed a semi-analytical model of the two dimensional accretion flow, and they found that the mass of the central protostar grows to at least $\gtrsim 30M_{\odot}$ to stop the mass

accretion.

Following the pioneering works, Hosokawa et al. (2011) tackled this issue by a two dimensional Radiation Hydrodynamics (RHD) simulation. As a result, they found that the mass accretion is shut off by the photoheating of the ultraviolet radiation from the protostar, when it grows to $43M_{\odot}$. Hirano et al. (2014) expanded the work to different one hundred cases, i.e. they picked up 100 minihalos from cosmological simulations, and followed the formation of the first stars in these halos by two dimensional RHD simulations. Consequently, they found that the final mass spreads in the range of $10M_{\odot} \lesssim M \lesssim 2000M_{\odot}$.

These are two dimensional calculations that can handle the radiation properly, although it is not possible to investigate the fragmentation of the gas disk. Thus, we need three dimensional calculations with radiative transfer in order to consider both of these effects. The three dimensional simulations of this type were first performed by Stacy et al. (2012). They solve the radiation transfer from the primary protostar, as well as the fragmentation of the disk. As a result, they found multiple stellar systems and an obvious sign of suppression of mass accretion onto protostars. However, they have integrated only five thousand years in physical time, which is not enough to obtain the final mass of the first stars.

In the wake of their works, Susa (2013) performed a three dimensional RHD simulation, in which radiation from all protostars are considered. They integrated the simulation until 10^5 yrs after the formation of the primary star, which enables them to assess the final mass of the first stars. They found five stars, in their particular simulation, in the range of $1M_{\odot} \lesssim M \lesssim 60M_{\odot}$, although they significantly underestimate the radiative feedback effect because of the insufficient resolution to capture the propagation of the ionization front. This mass range is, however, just one result from one realization. As pointed out by Stacy & Bromm (2013) and Hirano et al. (2014) we need a statistical study to obtain the correct mass range of the first stars, starting from cosmological simulations.

The mass range of the first stars is also important to clarify chemical evolution of the early Universe because nucleosynthesis in the first stars and their supernovae, which provides the first metal enrichment in the Universe, depends on their masses. The chemical evolution of the early Universe and the mass range of the first stars have been observationally constrained so far by means of observations of elemental abundances of metal-poor stars that formed in the early Universe (e.g., Beers & Christlieb 2005, for a review). In combination with theoretical studies of supernova nucleosynthesis and chemical evolution (e.g., Nomoto et al. 2013, for a review), the following consequences have been obtained: no chemical signature of a pair-instability supernova (PISN) yielding a peculiar abundance pattern has been found in the metal-poor stars (Heger & Woosley 2002; Umeda & Nomoto 2002) and the abundance patterns of the metal-poor stars are well reproduced by supernova explosions of first stars as massive as supernova progenitor stars in the present day ($M \lesssim 100M_{\odot}$) (Tominaga et al. 2007b; Heger & Woosley 2010). On the other hand, theoretical predictions based on cosmological simulations have not been available for the elemental abundance of the early Universe. This is because the

masses, i.e., initial mass function (IMF), of the first stars have not been well constrained.

In this paper, we perform cosmological simulations to obtain 59 minihalos that will host first stars. These halos are used as the initial conditions for long term RHD simulations of the first star formation. Based upon the results of the simulations, we derive the range of the stellar mass and the correlation between the stellar mass and the properties of the host minihalos/clouds. We also discuss the properties of the formed stellar systems in the minihalos, as well as their chemical imprints on the metal poor systems. This paper is organized as follows. We describe the method and setup of the numerical experiment in sections 2 and 3. Then we show the results of the simulations in section 4. Section 5 is devoted to discussion, and we summarize in section 6.

2. COSMOLOGICAL SIMULATION

In order to collect the samples of the minihalos that host the first stars, we perform cosmological hydrodynamic simulations using START (Hasegawa & Umemura 2010) that is an RHD code used in Hasegawa & Semelin (2013). We solve not only hydrodynamics but also non-equilibrium chemistry regarding H, H⁺, e⁻, H₂⁺, H⁻, H₂, He, He⁺, and He²⁺. The code can handle the ultraviolet radiation from various sources (Hasegawa, Umemura & Susa 2009; Umemura et al. 2012). However, in this work, we do not take into account the external radiation sources, in order to concentrate on the formation process of the so-called population III.1 stars. We will explore the impact of the external radiation sources on the minihalos and the mass spectrum of the first stars, i.e. the population III.2 stars in a forthcoming paper.

We employ a simulation box of 100kpc (comoving) on a side, which contains 2×512^3 SPH and DM particles. The initial conditions are generated by 2LPT code, in which the second-order Lagrangian perturbation theory is used, (Crocce, Pueblas, & Scoccimarro 2006) and all the simulations are initialized at $z = 200$. Throughout this paper we assume the Λ cold dark matter Universe with cosmological parameters of $\Omega_b = 0.049$, $\Omega_0 = 0.27$, $\Omega_{\Lambda} = 0.73$, and $h = 0.71$, based on 7-year WMAP results (Komatsu et al. 2011; Jarosik et al. 2011). We also adopt artificially enhanced normalizations of the power spectrum, $\sigma_8 = 1.5$, and 1.2 to accelerate the structure formation in the same manner as previous studies (e.g. Stacy et al. 2012). Hereafter, we call the former series of runs Runs A and the latter Runs B. We also perform a reference cosmological simulation with 2Mpc box containing 2×1024^3 SPH and DM particles, to check if the properties of the minihalos in Runs A/B are similar to those with a normal $\sigma_8 = 0.82$ in larger box.

In cosmological hydrodynamic simulations, we often suffer from the fact that a time step becomes very short during a density peak is collapsing, because of the very short thermal time scale at the peak. Consequently, it is difficult to extract several samples of minihalos from a cosmological run. In order to avoid such a difficulty, we employ a procedure described below. In each run, we adopt a threshold density n_{th} . When a density peak reaches n_{th} , we extract and store the data of all the physical quantities around the peak, i.e. the data of a minihalo. Then we convert all of the SPH particles that re-

side within 150pc from the density peak, into collisionless particles, retaining the information of the positions and velocities of the particles. Thus, the very short thermal time scale around the density peak is safely ignored that allow the other minihalos to collapse. We also note that the halos composed of the collisionless particles could merge with neighboring non-collapsed halos, although such events are very rare. We never extract halos which are contaminated by the the collisionless particles when the halos collapse. In fact, we find only five cases of such merger event in all of the Runs A/B. Hence, neglecting the contaminated halos hardly affects our results.

Owing to this procedure, we can alleviate the difficulty caused by shortened time steps, and extract multiple minihalos from each run. We set $n_{\text{th}} = 10^8 \text{cm}^{-3}$ for both of the Runs A and B, and $n_{\text{th}} = 10^3 \text{cm}^{-3}$ for the reference run.

We note that the minihalos found in the reference run are never used for the subsequent RHD simulations (see section 3 for more details), since the DM potential well seems to be still non-negligible when the density peaks reach $n_{\text{th}} = 10^3 \text{cm}^{-3}$ (Abel et al. 2002). We carry out 24 runs of Runs A and 17 runs of Runs B, and extract 59 halos from the runs. The characteristics of the cosmological simulations are summarized in Table 1.

3. THE LOCAL SIMULATION OF FIRST STAR FORMATION

3.1. RHD simulation

We pick up 59 minihalos from the cosmological simulations, then follow the subsequent evolution by local RHD simulations. Each SPH particle in the minihalos is split into ten SPH particles in order to achieve sufficient resolution to resolve the fragmentation at 100 – 1000AU scales. As a result, the mass of an SPH particle in the local simulations is $m_{\text{SPH}} = 5 \times 10^{-3} M_{\odot}$ which corresponds to the mass resolution of $0.5 M_{\odot}$ ($= 2N_{\text{neib}} m_{\text{SPH}}$), where N_{neib} ($= 50$) is the number of neighbor particles (Bate & Burkert 1997). We perform local simulations starting from these initial conditions.

The code we use to simulate the systems is RSPH (Susa & Umemura 2004; Susa 2006; Susa & Umemura 2006) with some extensions (sink particles, updated rates, cooling rates at high density, time stepping) described in Susa (2013). Utilizing the code, we solve the hydrodynamics, non-equilibrium primordial chemistry of six species, e^- , H^+ , H , H_2 , H^- , H_2^+ , and radiative transfer of ultraviolet photons in this numerical experiment. RSPH is a code that solve hydrodynamics by SPH scheme, and the radiation transfer by ray-tracing. The ray-tracing from a point source is realized by connecting neighbor particles using the neighbor list of SPH method (Susa 2006). The ray-tracing enables us to calculate the optical depth at the Lyman limit as well as the H_2 column density from any source star to each SPH particle. We remark that the resolution of the present simulations is not enough to capture the propagation of the ionization front, although the photoionization/photoheating is implemented to the code (see 4.1 and 5.1). H_2 column density is also used to calculate the self-shielding function of Lyman-Werner (LW) photons (Wolcott-Green et al. 2011). H_2^+ photodissociation is also taken into account, based upon the cross-section in Stancil (1994). H^- radiative detachment is

assessed using the fitting formula for the cross-section in Tegmark et al. (1997).

We take into consideration the standard cooling processes of primordial gas such as H/H_2 line cooling, H_2 formation heating/dissociation cooling, H ionization/recombination cooling, bremsstrahlung, optically thin H^- cooling and collision induced emission cooling. Optically thick H_2 line cooling is taken into consideration by using the simple analytic formula shown as the equation (22) in Ripamonti & Abel (2004). In the present version of RSPH code based upon Susa (2013), we update the hydrodynamics, gravity, and radiative transfer at the time step given by the Courant condition, while the energy equation and chemical reaction equations are integrated at smaller time steps.

We remark that we only simulate the central spherical region with radius 0.6pc in the cloud, after the formation of the first sink in order to save the computational time. The outer envelope of $r > 0.6\text{pc}$ is omitted from the calculation since it hardly affects the evolution of the inner region within 10^5yrs .

3.2. Sink particles

A sink particle technique is employed in the present simulations, which is the same as the one employed in Susa (2013). We search the highest density peak at every time step. Then corresponding SPH particle is converted into a sink particle if the peak density exceeds a threshold density, $n_{\text{sink}} = 3 \times 10^{13} \text{cm}^{-3}$. We also set an accretion radius as $r_{\text{acc}} = 30\text{AU}$. If the distance from a sink particle to an SPH particles is less than r_{acc} and they are gravitationally bound with each other, the SPH particle is merged to the sink particle, conserving the linear momentum and the mass. These sink particles are regarded as protostars in this experiment.

The sink-sink merging is not allowed in the present numerical experiment, because the actual protostellar radius is much smaller than r_{acc} . In fact, the radius of the protostar is less than $\sim 1\text{AU}$ (Hosokawa & Omukai 2009) even at the maximally expanded phase just before Kelvin-Helmholtz (KH) contraction. However, we have to keep in mind that merging between the protostars should be properly taken into consideration at much higher resolution studies (e.g. Greif et al. 2012; Machida & Doi 2013).

We also assume that the sink particles behave as “black holes”, i.e. they interact with surrounding particles as only sources of gravity (and radiation, discussed later). In other words, the pressure forces from sink particles to surrounding SPH particles are omitted. The recipe of the sink particles employed in the present work is known to overestimate the mass accretion rate (e.g. Bate et al. 1995; Bromm et al. 2002; Martel et al. 2006). Combined with the fact that the accretion radius is much larger than the protostellar radius, the resultant mass of the formed sink particles would be larger than the actual mass of the first stars.

We stop the simulation at 10^5yrs after the first sink formation, which is longer integration time than the two dimensional RHD simulation by Hosokawa et al. (2011).

3.3. Protostellar evolution model

We turn on the sinks, i.e. protostars, when they are created. In order to obtain the luminos-

TABLE 1
CHARACTERISTICS OF COSMOLOGICAL RUNS

Series	L_{box} [Mpc]	$N_{\text{SPH}} (=N_{\text{DM}})$	m_{DM} [M_{\odot}]	m_{SPH} [M_{\odot}]	σ_8	N_{halos}	n_{th} [cm^{-3}]
Runs A	0.1	512^3	0.25	0.049	1.50	38	10^8
Runs B	0.1	512^3	0.25	0.049	1.20	24	10^8
Reference	2.0	1024^3	250	4.90	0.82	1878	10^3

ity/spectrum of the source protostars found in the simulations, we have to employ a protostellar evolution model. These properties of a protostar is obtained based on the calculation by Hosokawa & Omukai (2009). They have calculated the steady evolution of the protostars (Stahler et al. 1986) with given (fixed) mass accretion rates. We use their numerical data of $\dot{M}_* = 4 \times 10^{-3}, 10^{-3}, 10^{-4}$ and $10^{-5} M_{\odot} \text{yr}^{-1}$, and analytic formula for $\dot{M}_* > 0.1 M_{\odot} \text{yr}^{-1}$. Intermediate cases are interpolated between the data. The analytic formula for high mass accretion rate is given by Hosokawa et al. (2012). The analytic formulae are given in the two phases, i.e. the mass accretion phase and the KH contraction phase. The protostars normally evolve from the former to the latter, and the phase changes when the mass of the protostar exceeds $M_{*,\text{teq}}$. This corresponds to the time when the mass accretion time scale, t_{acc} equals to the KH contraction time scale, t_{KH} (e.g. Hosokawa et al. 2012). These quantities are defined as:

$$M_{*,\text{teq}} = 14.9 M_{\odot} \left(\frac{\dot{M}_*}{10^{-2} M_{\odot} \text{yr}^{-1}} \right)^{0.26}$$

$$t_{\text{acc}} = \frac{M_*}{\dot{M}_*}$$

$$t_{\text{cool}} = \frac{GM_*^2}{R_* L_*}$$

where R_* , L_* , M_* and \dot{M}_* denote the radius, the luminosity, the mass and the mass accretion rate of the protostar, respectively.

For the mass accretion phase ($M_* < M_{*,\text{teq}}$) the analytic formula reads,

$$R_* = 26 R_{\odot} \left(\frac{M_*}{M_{\odot}} \right)^{0.27} \left(\frac{\dot{M}_*}{10^{-3} M_{\odot} \text{yr}^{-1}} \right)^{0.41}$$

$$L_* = \frac{GM_* \dot{M}_*}{R_*}$$

In KH contraction phase ($M_* > M_{*,\text{teq}}$), we have

$$R_* = 2.6 \times 10^3 R_{\odot} \left(\frac{M_*}{100 M_{\odot}} \right)^{1/2}$$

$$L_* = 3.8 \times 10^6 L_{\odot} \left(\frac{M_*}{100 M_{\odot}} \right).$$

Fig.1 shows the color contour of R_* as a function of M_* and \dot{M}_* . The lower right black-purple region corresponds to the parameter space where the protostar is settled onto the main sequence stars emitting UV radiation, whereas the top orange-yellow region is no UV emitting high mass accretion branch found by Hosokawa et al. (2012). The

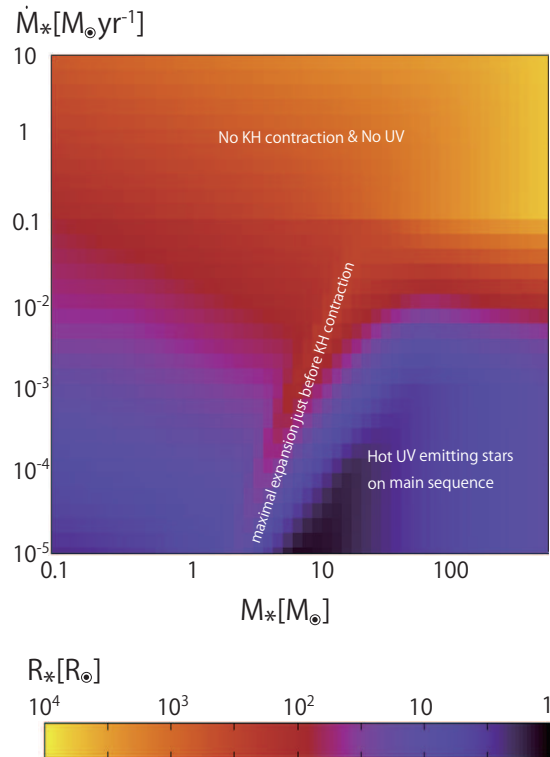


FIG. 1.— Color contour of protostellar radius on $M_* - \dot{M}_*$ plane.

ridge line found in the lower middle region denotes the maximal expansion phase of the protostar just before the KH contraction. We assume the spectrum of the protostar is black body, and the effective temperature of the protostar is obtained by the equation $L_* = 4\pi R_* \sigma T_{\text{eff}}^4$. We also have similar contour map of L_* , thereby we can derive the luminosity and spectrum of a protostar with given M_* and \dot{M}_* ¹.

On the other hand, we can assess the protostellar mass (M_*) and the mass accretion rate (\dot{M}_*) self-consistently from the hydrodynamics simulation. The mass accretion rates onto the sinks in the present simulation are obtained by averaging over 10^3 yrs in order to avoid artificial jumps due to SPH discreteness. These quantities are fed to the protostellar evolution model described above at every time step, which in turn gives the luminosity and spectrum of protostars used in the simulation at the next step. Hence, the protostellar evolution model is self-consistently taken into account in the radiation hy-

¹ We have to keep in mind the limitation of this procedure. In case the mass accretion is very stochastic and changes much faster than the KH contraction time scale, this procedure is not sufficient to trace the evolution of the protostar. In the present simulations, the mass accretion rate is smoothed over 10^3 yrs, which is longer than the KH contraction time scale during the UV emitting phase of protostars. Thus, the present treatment is self-consistent.

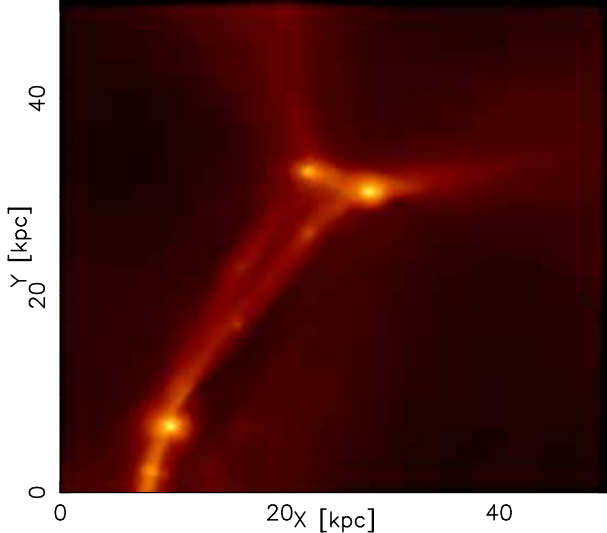


FIG. 2.— Projected gas density distribution in one of Runs A at $z = 14.0$. The presented volume is 1/8 of the whole box of this run. The three density peaks in the map are extracted as the hosts of the first stars.

drodynamics calculations.

4. RESULTS

4.1. Properties of the minihalos

In this section, we describe the properties of the minihalos found in the cosmological simulations. In order to quantify the properties of the dark matter halos, we define the region, whose mean mass density inside a certain radius from a density peak corresponds to 200 times the average mass density of the Universe, as a virialized halo. Then we define the mass inside the radius, called virial radius r_{vir} , as the virial mass M_{vir} . In addition, when the density peak of a halo reaches n_{th} , we regard the halo as collapsed. We estimate the spin parameter of a halo using the following formula,

$$\lambda_{\text{vir}} = \frac{j_{\text{vir}}}{\sqrt{2GM_{\text{vir}}r_{\text{vir}}}}, \quad (1)$$

where j_{vir} is the specific angular momentum of the halo.

In Fig. 2, we show the zoomed map of the projected gas density at $z = 14$ from a run with $\sigma_8 = 1.5$ (Runs A). In this case, we find three minihalos (three bright spots in the map) that host first stars.

In Fig. 3, we show the frequency distributions of the halo virial mass, the spin parameter, and the collapse redshift obtained by our simulations. In each panel of the figure, the heights of the histogram is normalized by the total number of the halos. It is needless to say, the halos in Runs A tend to collapse earlier than those in Runs B because of the difference of the mean heights of density peaks. We also can see that the halos in Runs A are relatively less massive than those in Runs B. This trend also can be understood by the fact that the first star forming halos have to be cooled by the H_2 cooling process, which can only be important if the temperature of the collapsing gas clouds exceed 1000 – 2000K. Since the maximal gas temperature is basically determined by the virial temperature of the halos, which is proportional to $M_{\text{vir}}^{2/3}(1+z_{\text{col}})$, the star forming minihalos collapse at lower redshift are more massive to meet the condition of

virial temperature.

We also notice that the spin parameters for the halos in Runs B is slightly higher than that in Runs A. This seems to originate in the fact that higher density perturbations reach their turn around time earlier, thereby their spin-up time tends to be shorter (Steinmetz & Batelmann 1995). As argued in the above, our samples of minihalos are qualitatively consistent with the theoretical predictions.

We also tested if the properties of the minihalos in Runs A/B are similar to those found in the reference run. The volume in the reference run is 8000 times larger than that of Runs A/B, and the employed σ_8 is 0.82 which is the ordinary value in WMAP 7-year cosmology. Thus, the reference run would give proper average distribution of minihalos, although it lacks the mass resolution required for the initial conditions of the local RHD simulations. We note that the reference run is stopped at $z = 9$ to save the computational time. We pick up 1878 minihalos that will host first stars in the reference run, and the results are superimposed on the panels of Fig. 3. Consequently, we find that the frequency distribution of the minihalos picked up from the boosted σ_8 runs (Runs A + Runs B, blue dotted line “ALL”) are consistent with those with the normal σ_8 for $z > 9$. The chief reason would be that the first star forming minihalos form at the high- σ density peaks even in the larger box, which makes the properties of the minihalos in the reference run to be similar to those in Runs A/B.

In Fig. 4, we show the number density and specific angular momentum as a function of enclosed mass, and the gas temperature and hydrogen molecular fraction as a function of number density. Here, we emphasize two important points in this figure. First, these internal properties of our samples are similar to those in previous studies (Yoshida et al. 2006; O’Shea & Norman 2007; Hirano et al. 2014). This also indicates that our samples are hardly affected by the enhanced normalization of the density fluctuations. Second, the properties of the halos shown in the figure show large variations. These variations lead to the variety of clouds.

4.2. Properties of the cloud

We also define the dense “clouds”, the hosts of the first stars, located at the center of the gravitational potential of the minihalos, and show the properties of them. The definition of a “cloud” is the same as that adopted in Hirano et al. (2014). We take the snapshot when the peak density reaches $n_{\text{th}} = 10^8 \text{cm}^{-3}$, and average the physical quantities over the thin spherical shells, to obtain the radial distribution of them. Then we define the radius where the ratio of the enclosed mass to the local Bonner-Ebert (BE) mass takes the maximum as the cloud radius r_{cloud} ². Here the local BE mass is given by

$$M_{\text{BE}} = 1050 \left(\frac{T}{200\text{K}} \right)^{1.5} \left(\frac{\mu}{1.22} \right)^{-2.0} \left(\frac{n_{\text{H}}}{10^4 \text{cm}^{-3}} \right)^{-0.5} \left(\frac{\gamma}{1.66} \right)^{2.0} M_{\odot}, \quad (2)$$

² We have to keep in mind that this definition could introduce artificially large cloud mass because it can pick up relatively distant radius when multiple density peaks are present.

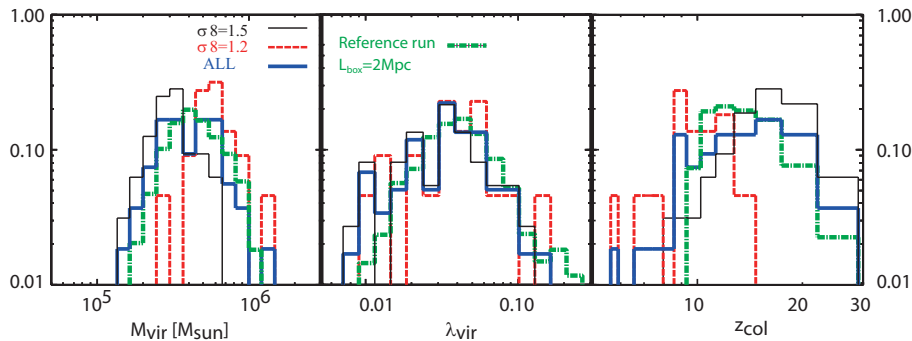


FIG. 3.— Frequency distributions of the virial mass, spin parameter, and collapse redshift of halos. In each panel, the result of Runs A, and Runs B are respectively indicated by the thin solid and dashed lines. Also, the results for all halos, namely combined data of Runs A and Runs B, are shown by the thick solid lines. The results of the reference run are indicated by the dot-dashed lines.

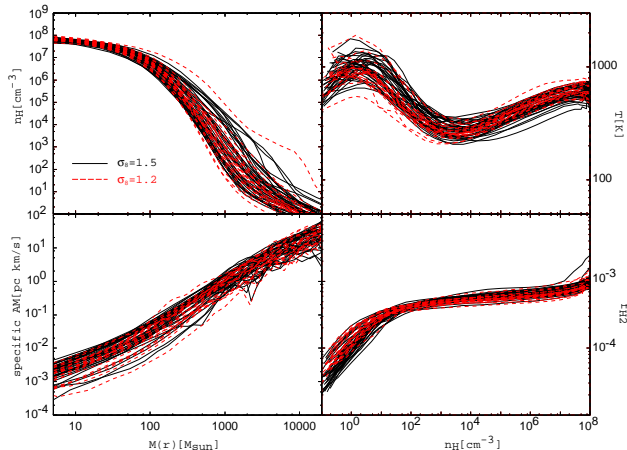


FIG. 4.— Number density as a function of enclosed mass (upper left), specific angular momentum as a function of enclosed mass (lower left), gas temperature as a function of number density (upper right), and H_2 fraction as a function of number density (lower right). In each panel, the Runs A and Runs B halos are indicated by the solid and dashed curves, respectively.

where μ and γ are the mean molecular weight and the adiabatic index, respectively. Once we determine the cloud radius r_{cloud} , the cloud mass is defined as the enclosed mass within r_{cloud} . The cloud radius (r_{cloud}) roughly corresponds to the radius where $n_H \simeq 10^4 \text{cm}^{-3}$ is satisfied. The spin parameter of a cloud is estimated by the equation(1), replacing the subscript of "vir" with "cloud". The mass infall rate at a cloud surface is defined as

$$\dot{M}(r_{\text{cloud}}) = 4\pi r_{\text{cloud}}^2 \rho(r_{\text{cloud}}) v_{\text{rad}}(r_{\text{cloud}}), \quad (3)$$

where $v_{\text{rad}}(r)$ and $\rho(r)$ are the radial velocity and gas mass density averaged over a thin shell at a radius r , respectively.

We show the frequency distributions of the cloud mass, the spin parameter, and the infall rate at the surface of the cloud in Fig. 5. As expected from Fig. 4, we can see large variations in the properties of the clouds. Also, it is important to remark that the fraction of less massive cloud with $M_{\text{cloud}} < 100M_{\odot}$ is smaller than that in Hirano et al. (2014). They found $\sim 1/3$ of the minihalos host such less massive clouds. It likely originates in the lack of HD cooling in our simulations. As pointed out by Hirano et al. (2014), HD cooling would be important for our sampled halos that cool down to $T \approx 200\text{K}$.

The mean spin parameter of clouds in Runs A is slightly higher than that in Runs B, in contrast to the

fact that mean spin parameter of halos in Runs A is slightly lower than that in Runs B. It is not simple to give a comprehensible reason for the trend, since the angular momentum of the central baryonic component is determined at much smaller scale than the halo scale.

4.3. An example among the local simulations

We obtain 59 minihalos that are going to host first stars from the cosmological simulations as described above. The next step is to perform local RHD simulations of first star formation using these minihalos as the initial conditions. In this section, we show the results of a particular case among these minihalos in which the low mass stars form as did in the case shown in Susa (2013). The present result is consistent with that of Susa (2013).

In Fig.6, we show the density distribution of the gas within $2000\text{AU} (= 10^{-2}\text{pc})$ in radius around the primary first star at three epochs (hereafter we call the most massive star at the final phase primary star). The color denotes the density, while the small spheres represent the positions of the sink particles, and their radii are proportional to the mass of the sinks. In the early phase of the mass accretion (2180yr after the first sink, top), dense accretion disk form around the primary star, and we find a prominent spiral structure as was also found in previous works (e.g. Susa 2013). After a while, the spiral arms fragment into sink particles, and the gas density surrounding the sink particles decline because of the radiative feedback from the stars (8180yr, middle). Finally, the gas density around the sink particles becomes much lower than the initial disk, that will limit the further mass growth of the sinks (98780yr, bottom). The masses of the sinks at the final stage of the simulation are in the range of $4M_{\odot} \lesssim M_* \lesssim 40M_{\odot}$.

Fig.7 shows the number density of the gas n_H (top), the gas temperature (middle), and the H_2 fraction y_{H_2} (bottom) as functions of the distance from the primary star. Each dot corresponds to an SPH particle, and the three colors represent three snapshots at different epochs which are equivalent to those in Fig.6.

In the early phase, 2180yrs after the formation of the primary star, an accretion disk of $n_H \simeq 10^{12}\text{cm}^{-3}$ forms at inner $10^{-3}\text{pc} (\simeq 200\text{AU})$ region (top, red dots). The temperature of the disk is $\lesssim 1000\text{K}$ (middle, red dots) and it is fully molecular (bottom, red dots). We also observe less dense particles of $10^{10} - 10^{11}\text{cm}^{-3}$ at $r < 10^{-3}\text{pc}$

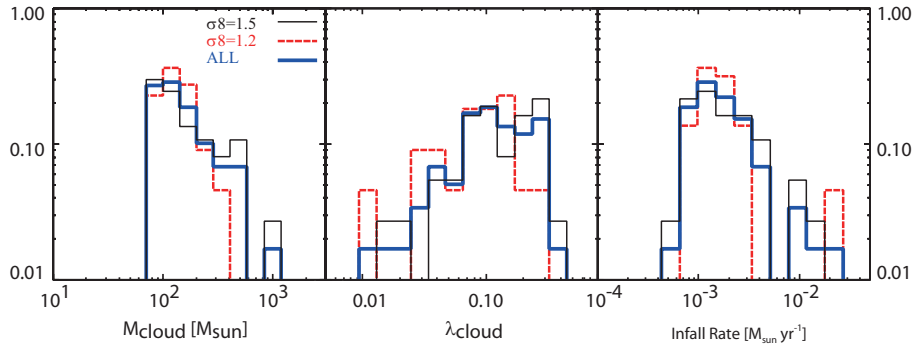


FIG. 5.— Frequency distributions of the mass, spin parameter, and infall rate of clouds. In each panel, the result of the Runs A, and Runs B are respectively indicated by the thin solid and dashed lines. Also, the results for all halos, namely the combined data of Runs A and Runs B, are shown by thick solid lines.

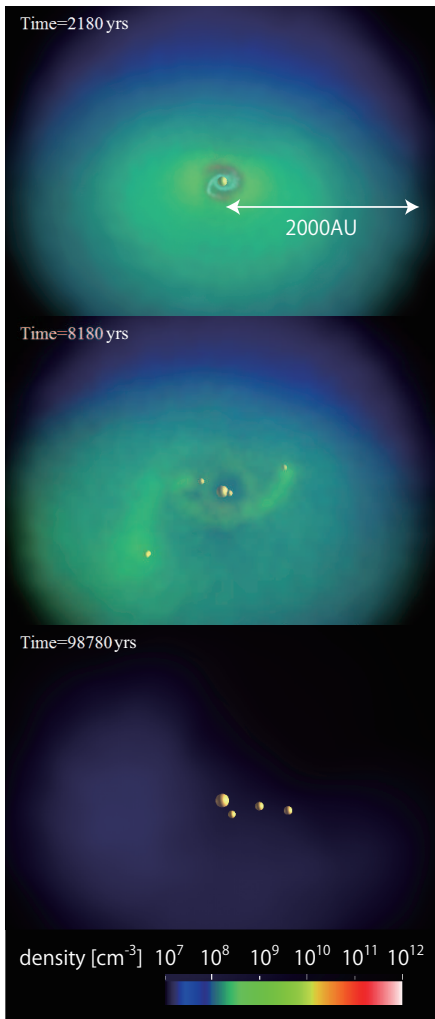


FIG. 6.— Density distributions at three snapshots, 2180 yrs, 8180 yrs and 98780 yrs after the formation of the primary star by pseudo volume rendering. White spheres represent the sink particles, and the size is proportional to their mass.

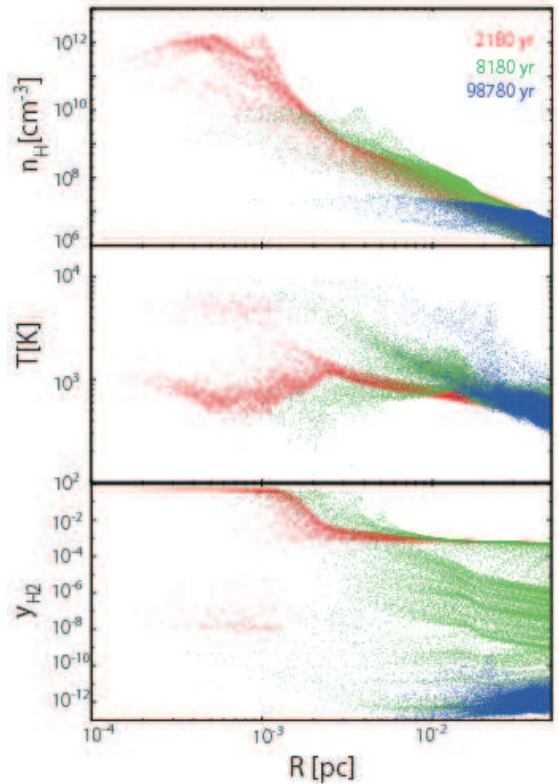


FIG. 7.— Density (top), temperature (middle) and H_2 fraction (bottom) are shown as functions of the distance from the primary star for a typical minihalo. Each dot corresponds to the SPH particle. Three colors correspond to three snapshots at 2180 yrs, 8180 yrs and 98780 yrs after the formation of the primary star.

(top, red dots), these are located on the polar region of the primary star. The temperature of these gas particles are as low as several $\times 10^3 K$, and H_2 molecules are dissociated. The gas is heated by the chemical heating of H_2 formation process which is prominent because of the presence of the photodissociative radiation from the protostar (Susa 2013, see also section 5). We also note that Turk et al. (2010) reported the importance of chemical heating even before the protostar formation. As time proceeds, the gas density around the central protostar is getting lower and lower (top, green/blue dots), and the temperature is kept around $10^3 K \lesssim T \lesssim 10^4 K$ (middle, green/blue dots). At the final stage, the gas is totally dissociated and the density is as high as $10^7 cm^{-3}$.

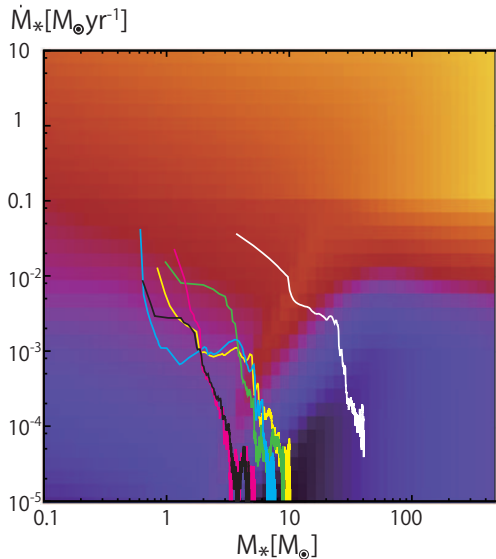


FIG. 8.— Evolution of sink particles on the $M - \dot{M}$ plane. The color gradient is same as Fig.1. Solid lines denote the path of the six sink particles in this particular run.

Fig.8 shows the evolution of the six sink particles born in this particular case on the $M_* - \dot{M}_*$ plane. The final mass of the primary one is as large as $40M_\odot$, while the others are $\lesssim 10M_\odot$. The final mass accretion rates are $\dot{M} \lesssim$ a few $\times 10^{-5}M_\odot \text{ yr}^{-1}$, which is much lower than the initial rate of $10^{-2} - 0.1M_\odot \text{ yr}^{-1}$ because of the radiative feedback effects. In addition, the mass accretion rate at such later phase would be lower than this value, if we could take into consideration the photoionization feedback properly (Hosokawa et al. 2011), since the ionized gas has higher temperature.

We also remark that the primary and the secondary have already settled down to the main sequence phase at 10^5 yr . The rest of the low mass stars are uncertain, since it is not possible to resolve the mass accretion rate $\lesssim 10^{-5}M_\odot \text{ yr}^{-1}$, above which the stars of $\lesssim 10M_\odot$ are still in the pre-main-sequence phase. We also have checked that all of the protostars more massive than $10M_\odot$ found in 59 minihalos are in the main sequence phase by the end of the simulation, i.e. 10^5 yrs after the first sink formation.

4.4. Mass spectrum

We perform local radiation hydrodynamics simulations starting from the 59 minihalos found in the cosmological simulations. Hence we obtain the mass spectrum of the stars by summing up the contributions from all the minihalos. In the mass spectrum of Fig. 9, all the stars found in the local simulations are taken into account.

It is immediately obvious that we have a very top heavy mass spectrum with a peak at several tens of solar mass, and most of the first stars are within the range of $10M_\odot \lesssim M \lesssim 100M_\odot$. This is the first IMF of the first stars by way of the three dimensional simulations including the effects of the radiative feedback and the fragmentation.

On the other hand, stars exceeding $140M_\odot$, i.e. the progenitors of PISNe also exist in the simulations. In fact, those very massive stars account for $\sim 20\%$ of the total mass accreted onto the stars found in the simula-

tions. However, as will be discussed in section 5, the effects of the radiative feedback tend to be underestimated in the present simulations. Thus, the high mass end of the present mass spectrum could be larger than the real spectrum. Thus, number of stars of exceeding $140M_\odot$ presumably smaller than the present results, and the mass fraction of 20% should be regarded as an upper limit.

We also mention that we do not find the case where very massive stars of $> 300M_\odot$ form unlike those found by Hirano et al. (2014). The branch to form such stars requires very high mass accretion rate of $\gtrsim 10^{-2}M_\odot \text{ yr}^{-1}$ all through the growth of the protostar. This short mass accretion time scale does not allow the KH contraction of the protostar, which inhibits the ultraviolet radiative feedback. In the present calculations, the mass accretion rate onto each star does not stay at such a high value. One possible reason is the fragmentation of the accretion disk, which simply reduces the mass of the primary stars. In addition, the mass accretion rate onto a star is also reduced, which makes the mass accretion time scale longer. As a result, the radius of the protostar shrinks to emit ultraviolet radiation, and the radiative feedback reduces the mass accretion rate. As for the case of single stars the gas infall rate onto the clouds are $\sim 10^{-3}M_\odot \text{ yr}^{-1}$ in our samples. The mass accretion rate onto the star is even smaller than this rate, which is less than the threshold mass accretion rate. Thus, the single stars found in our calculations do not trace the track of the very high mass accretion rate. The small sample size of our simulations could lead to such an absence of clouds with very high infall rate. But we also point out that even if we have the case of very high mass accretion rate, the non-axisymmetry could cause the fragmentation, which result in the formation of lower mass stars. In any case, we do not find the branch of the very massive star formation with high mass accretion rate in our samples.

We also find the stars of \lesssim a few $\times M_\odot$, although they occupy relatively small fraction. We have to be careful to interpret this result, since we do not have enough resolution to study the formation of such low mass stars. In fact, we assume the accretion radius of 30AU, which does not allow the fragmentation of the disk within 30AU. According to numerical experiments with very high resolution (but very short integration time), the accretion disk within 30AU does fragment into many clumps, and significant fraction of them are kicked away from the high density region via three body interaction (e.g. Greif et al. 2012; Machida & Doi 2013). Such stars seem unlikely to grow significantly, since the mass growth rate should be smaller in less dense environments. Considering these theoretical evidences, the mass spectrum obtained by our simulations could underestimate the number of low mass stars, although it is very difficult to assess the number correctly as matters now stand.

The colors of the histogram denote the order of the birth of the stars. It is clear that the earlier they form, the more massive they become. We also find that the majority of the high mass stars of $\gtrsim 30M_\odot$ are the primary stars, whereas the low mass stars of $\lesssim 30M_\odot$ are not. This is because the radiative feedback effects become significant after the primary star grows to 20–30 M_\odot , otherwise the mass accretion is not hindered by the radiation.

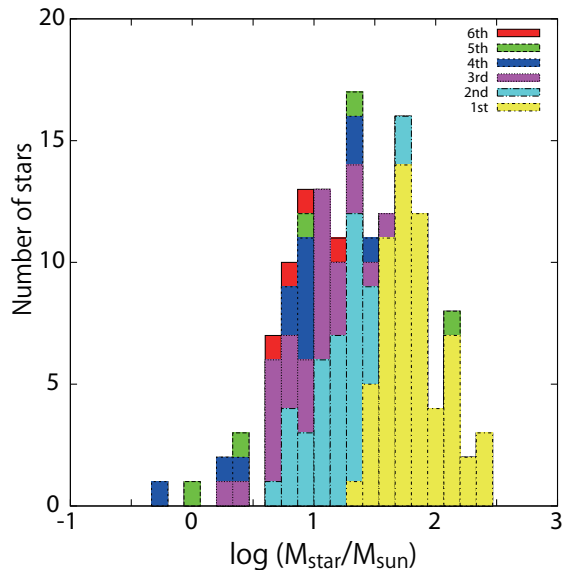


FIG. 9.— The mass spectrum of first stars is shown. Colors in the histogram correspond to the order of birth of these stars. The color legend in the upper right corner describes the correspondence between the order of birth and the color.

Here we mention the “final mass” in our simulations. The mass accretion rate at 10^5 yr is low, but is not completely zero. The typical mass accretion rates onto the massive stars of $\gtrsim 100M_\odot$ are $\sim 10^{-4} - 10^{-3}M_\odot\text{yr}^{-1}$. In such cases the mass extrapolated to 1Myr is a factor of two larger than the mass at 10^5 yr. On the other hand, the mass accretion rates of $10^{-4} - 10^{-3}M_\odot\text{yr}^{-1}$ are lower than the threshold rate ($10^{-2}M_\odot\text{yr}^{-1}$) above which the mass accretion could continue avoiding the photoionization feedback (Hosokawa et al. 2012; Hirano et al. 2014). Thus in the present simulations, the photoionization feedback should kick in if we have enough resolution to resolve the propagation of the ionization front. We have performed a very long term simulation for a minihalo that hosts single $170M_\odot$ star at 10^5 yr to check this conjecture. As a result, we find the inner region of the gas is fully ionized and the mass accretion totally stops at $\sim 6 \times 10^5$ yr, when the ambient gas density becomes as low as $\text{several} \times 10^6\text{cm}^{-3}$ and the stellar mass is $295M_\odot$. In fact, the Strömgen radius at this density ($1.2 \times 10^3\text{AU}$) and the SPH size ($5.6 \times 10^2\text{AU}$) are comparable with each other. This photoionization feedback should come into play at much earlier epoch if we have enough resolution. Actually, the photoionization feedback shut off the mass accretion at 8×10^4 yr in a particular grid simulation that can resolve the polar low density regions (Hosokawa et al. 2011). Hence, the mass accretion seemingly stops by $\sim 10^5$ yr also in our simulations if we could resolve the propagation of ionization front. Considering these evidences, we regard the mass at 10^5 yr as the final mass of the stars³.

4.5. Properties of multiple stellar systems

Fig.10 shows the multiplicity of the first stellar systems found in our numerical experiments. Approximately one-third of the 59 minihalos host single stars, while the rest

³ It is needless to say that we need RHD simulations with high enough resolution, though.

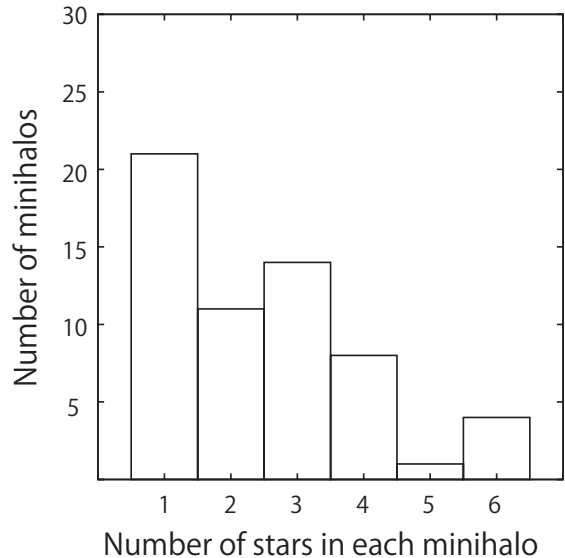


FIG. 10.— Multiplicity of the first stellar systems are shown. Vertical axis shows the number of minihalos while the horizontal axis is the number of the stars in those minihalos.

of the halos have more than two stars. As a result, the average number of stars in a minihalo is ~ 3 . We also note that if we employ sink-sink merging in our simulation, the multiplicity will decrease, although the assumption seems unlikely. In fact, the number of the sinks that experience the encounter with the other sinks satisfying the merging condition at least more than once is roughly $\sim 1/3$ of the total number of stars. But even with such a lax condition, the average number of stars per minihalo is ~ 2 . Thus, it is clear that fragmentation of the accretion disk to form multiple stars is a common phenomena among forming first stars in various minihalos. It is also worth noting that if we have better resolution inside 30AU, multiplicity will increase inevitably.

Fig.11 shows the mass of the primary star (M_1) in a minihalo v.s. the number of stars in the minihalo. It is clear that most of the stars with $> 140M_\odot$ are born as single stars in the present experiment, while the multiple systems scarcely contain such massive stars⁴. Thus, if second generation stars form from the ashes of these first stars in a single minihalo, we might be able to find the clear evidence of PISN in the abundance pattern of metal poor stars, which has not been found yet. We will come back to this point in section 4.7.

Fig.12 shows the budget of the average total stellar mass per minihalo versus the number of stars per minihalo. The yellow bars denote the averaged mass of the primary stars while other colors show the mass of the 2nd, 3rd, 4th, 5th and 6th stars, respectively (see the color legend). It demonstrates again that very massive stars are born as single stars, and the most massive stars in the minihalos are less than $100M_\odot$ on average in case they are born in multiple stellar systems. In addition, we also find that the second massive stars are also as massive as $20\text{-}30M_\odot$, which is massive enough to operate as the source of ultraviolet radiation. Thus, it is crucial to include the effects of radiative feedback from stars other than the primaries.

In Fig.13 we plot the distance from each star to the

⁴ We find only one exception.

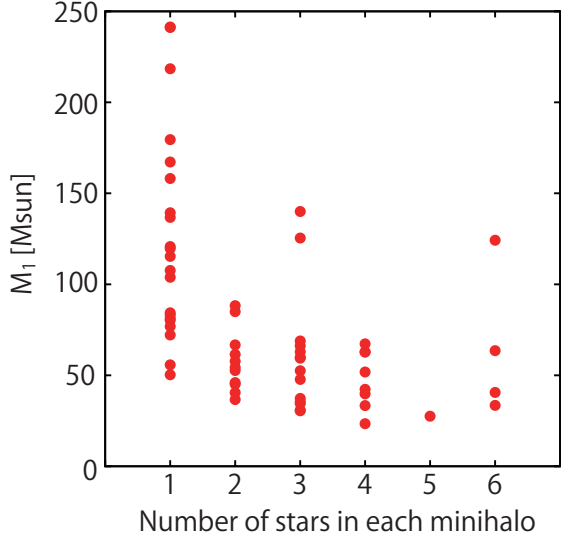


FIG. 11.— Mass of the most massive v.s. the number of stars in a minihalo.

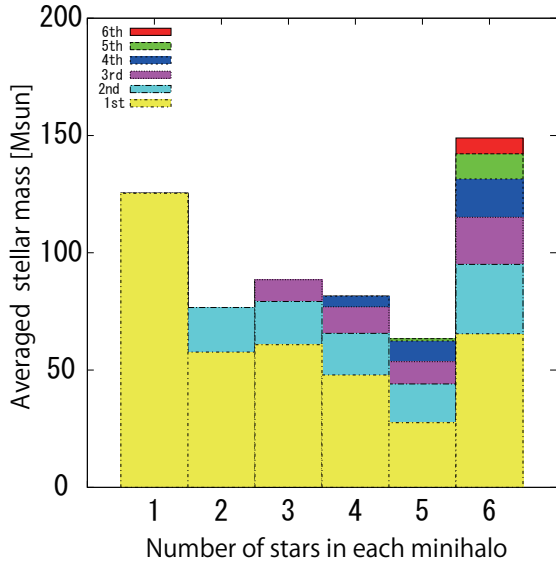


FIG. 12.— Averaged stellar mass in a minihalo. Horizontal axis is the number of the stars in those minihalos, while the vertical axis shows the stellar mass averaged over the minihalos which contain a given number of stars. The colors in the histogram denote to the fractions of the primary star (1st), secondary star (2nd), etc.

center of mass of the stellar system averaged over last 2×10^4 yrs. Only the stars in multiple systems are plotted. Open symbols denote the primary stars, while the filled symbols are the others. As a general trend, the distances from the center of mass widely spread over 4 orders of magnitude, i.e. form 10AU to 10^5 AU. Secondly, the stars located close to the center of mass tend to be massive, whereas the distant stars are less massive, although there are some outliers. This is because the low mass stars in multiple system tend to be kicked by the others via three body interactions. We also check the outward radial velocity of the relatively distant stars of $r > 10^4$ AU (~ 0.05 pc) to assess the possibility to escape from the host minihalos. The escape velocity of a typical minihalo is $4-5 \text{ km s}^{-1}$. We find only four of them exceed this limit. Since the total number of the minihalos found

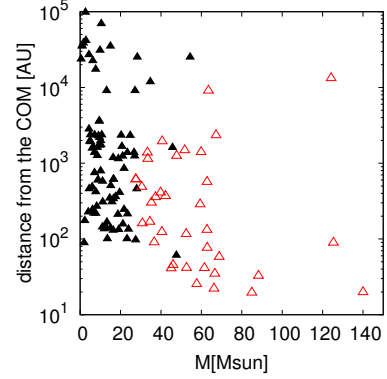


FIG. 13.— Averaged distance from the center of mass of the stellar system to the stars in the minihalos. Horizontal axis is the mass of the stars, while the vertical axis shows the distance from the center of mass of the stellar system, averaged over last 2×10^4 yrs. Open symbols denote the primary stars, while the filled symbols are others. We omitted the stars born as single stars in this figure.

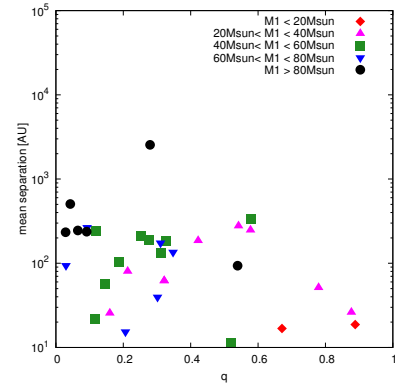


FIG. 14.— Averaged separation of the binaries found in the simulations. Horizontal axis is the ratio of the mass of the two stars, while the vertical axis is the separation of given pairs. The distance is averaged over last 2×10^4 yrs. The mass of the primary star is denoted by different symbols (see the legend).

in the present simulations is 59, the ejection rate from the minihalo is 0.067 star per minihalo. Thus the first stars born in a minihalo tend to stay within the dark halo potential. However, as seen in Fig.13, significant fraction of stars are wandering around 10^4-10^5 AU, which is very far from the central dense region. The stars kicked to the distant orbit when they are still not massive can hardly accumulate the gas, since the surrounding gas density is low. As a result, these stars cannot grow to massive stars. Thus, the gravitational three body interaction is important for the mass growth of the stars even if the ejection rate from the minihalo is very low.

We also try to find the binaries. We pick up all possible pairs of stars in each minihalo, and assess the total internal energy of the 2-body system as:

$$\epsilon = \frac{1}{2} \frac{m_1 m_2}{m_1 + m_2} (\mathbf{v}_1 - \mathbf{v}_2)^2 + \frac{G m_1 m_2}{|\mathbf{r}_1 - \mathbf{r}_2|} \quad (4)$$

where $m, \mathbf{v}, \mathbf{r}$ denote the mass, velocity and position of the stars respectively. The suffices 1 and 2 correspond to the members of the pair. In case this energy is always negative through the last 2×10^4 yrs of the simulation, we identify the pair as a binary. In Fig.14 the averaged separation of all binaries in the simulations are plotted against q , the mass ratio of the stars. Thus, each symbol

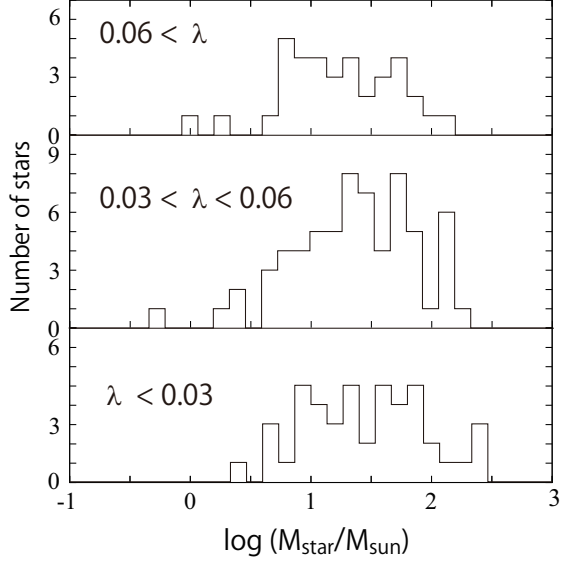


FIG. 15.— The mass spectrum of first stars at three different range of λ_{halo} .

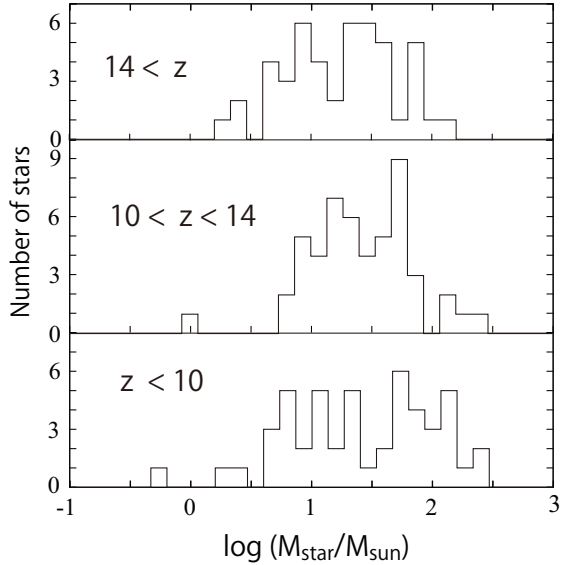


FIG. 16.— The mass spectrum of first stars at three different range of formation redshift.

denotes a binary in the simulation. The mass of the primary star of the binary is shown as the color and shape of the symbol. The mean separation of the binary system found in our simulation is $10 - 10^3 \text{AU}$. We also find a marginal trend that the pairs with more massive primary star has larger q . The total number of the binaries found in the simulation is 33, so the the frequency that a minihalo contains a binary system is $\sim 50\%$.

4.6. Correlation between the minihalo/cloud properties and the mass of the first stars

We explore the correlation between the minihalo/cloud properties and the mass of the first stars in this section. Here a “cloud” is the central dense region approximated as a Bonner-Ebert sphere as defined in section 4.1.

Fig.15 and 16 describe the dependence of the mass spectrum on the spin parameter and the formation epoch of the host minihalo. We separate the minihalos into

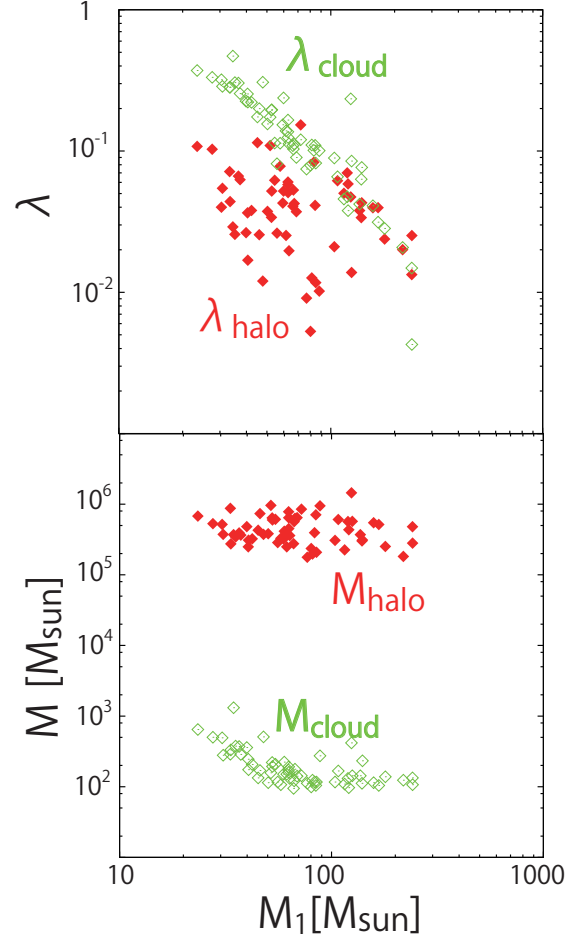


FIG. 17.— Top: The spin parameter of the minihalo λ_{halo} (red dots) and that of the gas cloud λ_{cloud} (green triangles) versus the mass of the primary star. Each symbol corresponds to each minihalo. Bottom: Same as top panel except the spin parameters are replaced by mass of the minihalo and the cloud.

three categories regarding the spin parameter and the formation redshift ($\lambda > 0.06, 0.03 < \lambda < 0.06, \lambda < 0.03, z > 14, 10 < z < 14, z < 10$) and draw the histogram for each bin. We find no significant dependence on the spin parameter and the formation redshift of the minihalos, although the number of stars is not sufficient to give definitive conclusions (see also Hirano et al. 2014; Stacy & Bromm 2014). This result implies that the mass spectrum of the first stars does not depend significantly on the environments, which allows us to use universal “IMF” for first stars in future cosmological simulations.

Fig.17 shows the correlation between the mass of the primary star M_1 and the spin parameter of the host minihalo/cloud (top panel), and the mass of them (bottom panel). Each symbol corresponds to each minihalo and cloud. First of all, we find that the mass of the primary star seems to correlate with the spin parameter of the cloud (λ_{cloud}). The relation is roughly $M_1 \propto \lambda_{\text{cloud}}^{-0.7}$. Although it is too complex to give analytical justification though, it is natural qualitatively: higher spin parameter inevitably results in larger disk and the gas needs to transfer more angular momentum outward to accrete onto the primary star. In addition, a larger disk tends to fragment to form secondaries. In fact, the averaged

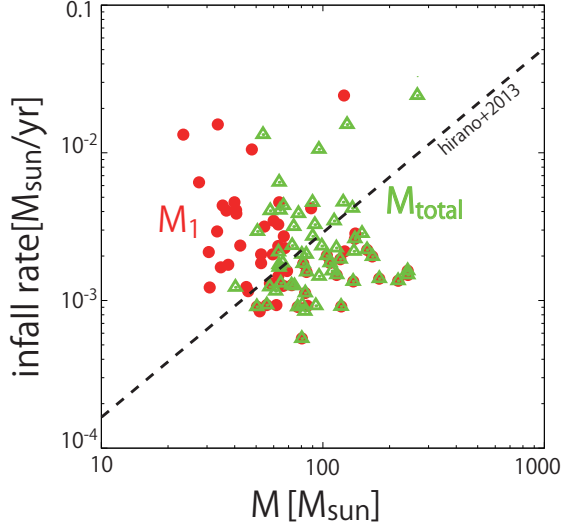


FIG. 18.— The mass infall rate versus the mass of the primary star (red dots) / the total stellar mass (green triangles). Dashed line shows the fitted relation between the mass of the central star and the infall rate found in the 2D simulations by Hirano et al. (2014).

λ_{cloud} over minihalos that host single stars is 0.065, while it is 0.20 if averaged over the halos that have multiple stars. On the other hand, we do not find significant correlation between the mass of the primary star and the spin parameter of the minihalo (λ_{halo}) as expected from the results in Fig.15. This result tells us that the correlation between λ_{cloud} and λ_{halo} is weak, because the central cloud is a much more concentrated inner system than the dark matter halo.

The bottom panel of Fig.17 shows the correlation between the mass of the primary star and the mass of the host minihalo/cloud. The mass of the minihalo is basically determined by the condition that the gas temperature is high enough to activate the H_2 cooling. Thus, the masses of the dark matter halos are almost identical ($M_{\text{halo}} \sim 10^5 - 10^6 M_{\odot}$) and seem unlikely to have correlation with the masses of the primary stars. On the other hand, as for the correlation with the cloud mass, we observe a weak trend that massive clouds host low mass primary. This trend reflects the weak correlation between λ_{cloud} and M_{cloud} . In our samples, clouds with high spin parameters, i.e. $\lambda_{\text{cloud}} \geq 0.1$, show a positive correlation between λ_{cloud} and M_{cloud} . However, the correlation might be misleading, since the cloud mass of high λ_{cloud} is often overestimated with our definition of the clouds. Except for such high-spin clouds, there is no clear correlation between λ_{cloud} and M_{cloud} .

In Fig.18 we plot the mass of the primary star (red dots) / total stellar mass (green triangles) versus the infall rate discussed in Hirano et al. (2014). Here the infall rate is defined by equation (3). They found that the infall rate well correlates with the mass of the central star in their 2D RHD simulations. It is not possible to compare the present results directly with those in Hirano et al. (2014), because their calculation does not take into account fragmentation. However, it is helpful to calculate the infall rate to understand the difference of two calculations. The dashed line denotes the fit given by Hirano et al. (2014), and red dots / green triangles are

the clouds found in our simulations. Both of the symbols (mass of the primary and the total mass) are not well correlated with the infall rate. The reason of this difference is unclear, but we guess that it mainly originates from the effects of fragmentation and the difference of the radiative feedback effect caused by the fragmentation.

4.7. Chemical imprints

The massive first stars explode as SNe and spread heavy elements into the surrounding gas, in which the next-generation stars form. While some of the next-generation stars also explode and contribute to further chemical evolution of the Universe, the elemental abundance of the gas enriched by the first stars remain in the long-lived low-mass stars or the gas which is not recycled to “third generation” stars. These system are likely to be found as metal poor systems in the present-day Universe, such as Extremely Metal Poor (EMP) stars/ Damped Lyman- α (DLA) systems. The abundance ratios of these systems preserve the nucleosynthetic results of the first stars. Thus, as intensively investigated in previous studies, the masses of the first stars can be verified by comparisons between the abundance pattern of the metal-poor systems and theoretical nucleosynthetic yields calculated from the IMF of first stars.

We derive theoretical yields with a stellar yield table that includes AGB stars, core-collapse supernovae (CCSNe), and PISNe (Nomoto et al. 2013),⁵ and the initial mass function of the first stars. The theoretical yields are compared with the observations of two metal-poor systems: (1) First is a metal-poor star that formed in the early Universe and is traditionally adopted to study the early chemical evolution (e.g., Yong et al. 2013). We adopt only normal metal-poor stars without enhancement of C or N because C-enhanced and N-enhanced metal-poor stars might require a specific type of CCSNe (faint SNe, e.g., Umeda & Nomoto 2002) and self enrichment in the low-mass metal-poor stars (e.g., Spite et al. 2005), respectively. (2) Second is a metal-poor damped Lyman- α (DLA) system that probes the gas-phase metal abundance at the distant Universe and is recently studied intensively (e.g., Cooke et al. 2013). Although the dust depletion could be an observational bias, it is suggested that the dust depletion is minimal at $[\text{Fe}/\text{H}] < -2$ (e.g., Pettini et al. 1997)⁶.

We test two cases of the initial mass function: the initial mass function derived in the previous sections (IMF1) and a modified initial mass function (IMF2), in which the mass of the first stars are reduced by a factor f . The IMF2 is a working hypothesis to understand how the obtained IMF (IMF1) overestimates the high mass end of the mass spectrum, due to the treatment of pressure from the sink particles and the inability of resolving the ionization front (see section 4.4 and 5). Here we choose 0.2 dex as f for a test case. The numbers of stars exploding as PISNe are 8 for Model IMF1 and 2 for Model IMF2, respectively. First of all, the total stellar

⁵ We assume that the stars with $20M_{\odot} \leq M \leq 140M_{\odot}$ explode as energetic CCSNe with explosion energy of $\geq 10^{52}$ ergs, called hypernovae.

⁶ Here $[A/B] = \log_{10}(N_A/N_B) - \log_{10}(N_A/N_B)_{\odot}$, where the subscript \odot refers to the solar value and N_A and N_B are abundances of elements A and B, respectively.

yield of all clouds is derived by integrating the mass dependent stellar yields over the initial mass function. The abundance pattern obtained here should be regarded as “a well mixed” case, where the remnant material in a minihalo is mixed with the others in a larger system.

Fig. 19 shows comparisons between the abundance pattern of the total yield of all clouds and the averaged abundance patterns of the extremely metal-poor stars with $[\text{Fe}/\text{H}] \sim -3$ (BD -18:5550, CS 29502-042, CS 29516-024, and CS 31082-001, Cayrel et al. 2004)⁷ and DLA systems (Cooke et al. 2011). We note that the chemical symbols indicated in gray denote the elements without observational data. In addition, the theoretical yields of the elements in cyan are known to suffer some missing ingredients in the stellar evolution/supernova model (rotation, mixing, neutrino, asymmetric explosion, etc., Nomoto et al. 2013). Thus we should pay attention on the elements printed as black in the present study.

The abundance pattern of Model IMF1 is not in agreement with that of EMP stars. The disagreements stem from the large contribution of PISNe in Model IMF1 and are improved in Model IMF2. The overall abundance pattern of the EMP stars is mostly reproduced by Model IMF2 even with 2 PISNe. This demonstrates that the peculiar chemical signatures of PISNe can be hidden by numerous CCSNe when the number of PISNe is small and the masses of PISNe are low.

Compared with the averaged abundance pattern of DLA systems, Model IMF1 and IMF2 present lower $[\text{C}/\text{Fe}]$ and higher $[\text{O}/\text{Fe}]$ than the observation, respectively, and they also exhibit over-abundance of Si due to the large contribution of massive stars with $M \gtrsim 50M_{\odot}$. These results might suggest that the DLA systems are contributed by stars with Salpeter’s initial mass function or a single Pop III CCSN as in Kobayashi et al. (2011). Indeed, the abundance ratios of an yield of a single minihalo contributed only by CCSNe and AGB stars is consistent with those of the DLA systems as shown below. We note that the disagreements on $[\text{N}/\text{Fe}]$ is improved by taking into account the rapid rotation of the first stars (Stacy et al. 2011).

We also consider cases with the IMFs in which the mass of the first stars are reduced by 0.1 dex and 0.3 dex ($f = 10^{0.1}, 10^{0.3}$). The former case is incompatible with the observed data as IMF1 is, whereas the latter is consistent. Thus, the high mass end of the IMF1 seems to be overestimated more than 0.2 dex if the abundance patterns of the low metallicity systems are mainly generated from the nucleosynthesis of the first stars. Here after, we only consider the case of $f = 10^{0.2}$ as a representative case.

Next, we consider the chemical enrichment in a single minihalo. The supernova explosions are so energetic that the ejecta is not confined in the minihalos (Kitayama & Yoshida 2005; Whalen et al. 2008), but the explosions themselves could induce second generation star formation by the compression of nearby density peaks or fragmentation of the shocked gas (Greif et al. 2007; Sakuma & Susa 2009; Chiaki et al. 2013; Dhanoa et al. 2014). If the EMP stars formed through such process, the abundance patterns reflect nu-

cleosynthesis of the first stars formed in each individual minihalo and their supernovae.

We simply assume that the SN yields are uniformly mixed with the gas in the minihalo and derive the yield integrated over each halo. The resultant $[\text{Fe}/\text{H}]$ of the halo is derived by the ejected Fe mass and the baryon mass of the halo.⁸ Fig. 20 compares $[\text{Mg}/\text{Fe}]$ and $[\text{Fe}/\text{H}]$ of the yield of each halo and those of metal-poor stars collected by SAGA database (Suda et al. 2011). Hereafter, LTE abundance ratios of the metal-poor stars are adopted. Since most of the massive stars exploding as PISNe form as single stars in the minihalos (Fig.11), the metals of such halos are produced only by the PISNe. As a result, their abundance ratio, low $[\text{Mg}/\text{Fe}]$ in Model IMF1 and high $[\text{Mg}/\text{Fe}]$ in Model IMF2, are not in agreement with those of the metal-poor stars, except for a halo with a $\sim 160M_{\odot}$ star in Model IMF1.⁹ The halos enriched by the AGB stars and the CCSNe are distributed in the range of $-3 \lesssim [\text{Fe}/\text{H}] \lesssim -2$ and show $[\text{Mg}/\text{Fe}] \sim 0.4$ which is consistent with $[\text{Mg}/\text{Fe}]$ of the metal-poor stars.

Figs. 21(a)-21(b) show the abundance ratios between metals, $[\text{Mg}/\text{Si}]$ and $[\text{Ca}/\text{Fe}]$, and $[\text{O}/\text{Fe}]$ and $[\text{Si}/\text{Fe}]$. Again, the abundance ratios of the halos enriched by the AGB stars and the CCSNe are consistent with those of the metal-poor stars, especially with the stars with $[\text{Fe}/\text{H}] < -3$ for the $[\text{Mg}/\text{Si}]$ and $[\text{Ca}/\text{Fe}]$ ratios, while the abundance ratios of the halos enriched by the PISNe are inconsistent with those of the metal-poor stars. It is worth noting that the $[\text{O}/\text{Fe}]$ and $[\text{Si}/\text{Fe}]$ ratios of a single minihalo of Model IMF2 are consistent with those of the DLA systems (see overlap of magenta box and cyan filled circle in lower-left region of panel (b)). The minihalo is enriched only by 5 less-massive CCSNe of stars with $M \lesssim 20M_{\odot}$ and an AGB star and also shows consistent $[\text{C}/\text{Fe}]$. We also note that the diversity of abundance ratios of the halos enriched by the AGB stars and the CCSNe are almost consistent with that of the metal-poor stars.

The first result of chemical enrichment based on the initial mass function of first stars suggests that the chemical imprints of PISNe can be hidden by the larger contribution from a number of CCSNe if the stellar yields are integrated over all halos and the masses of the first stars are reasonably reduced by a factor of 0.2 dex, although the chemical signatures of PISNe cannot be hidden in Model IMF1. This could be a solution for the long-standing problem that the contribution of PISNe is not found in the elemental abundances of metal-poor stars. However, we note that the chemical signatures of PISNe should be prominent if the second-generation stars form solely from the gas in the single minihalo, in which a PISN explodes, because such a massive star forms as a single star. The formation of second-generation stars could be constrained by future enhancement of the sample of metal-poor stars.

⁸ Here, we adopt the H mass fraction $X(\text{H}) = 0.7537$ as obtained from standard big bang nucleosynthesis (Coc et al. 2013)

⁹ According to Greif et al. (2007), $200M_{\odot}$ PISN can sweep $2.5 \times 10^5 M_{\odot}$, which is a few times larger than the averaged gas mass in the minihalos of our sample. Thus $[\text{Fe}/\text{H}]$ could slightly shift to the left especially for energetic explosions. But this will not help to improve the disagreement.

⁷ Non-LTE effects are taken into account as described in Tominaga et al. (2013).

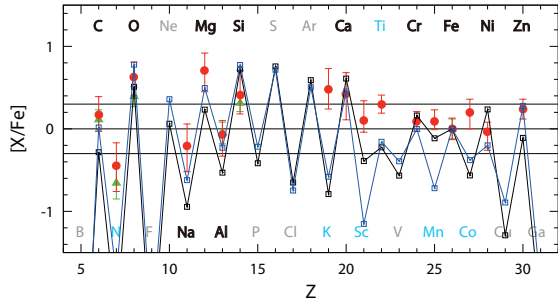


FIG. 19.— Comparison between the abundance patterns of the total yields of all clouds (*black*: Model IMF1 and *blue*: Model IMF2) and the averaged abundance patterns of EMP stars (*red*: Cayrel et al. 2004) and DLA systems (*green*: Cooke et al. 2011).

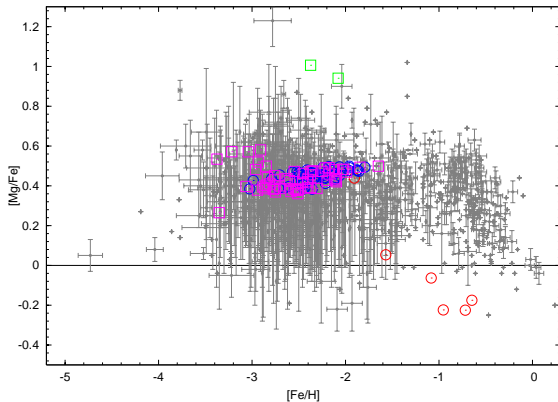


FIG. 20.— Abundance ratios, $[Mg/Fe]$ and $[Fe/H]$, of the yields of individual minihalos enriched by PISNe (*red*: Model IMF1 and *green*: Model IMF2) and CCSNe and AGB stars (*blue*: Model IMF1 and *magenta*: Model IMF2) and the metal-poor stars (*gray*, Suda et al. 2011)

5. DISCUSSIONS

5.1. Outstanding issues

In this paper, we perform the three dimensional radiation hydrodynamics simulations on the first star formation with long time integration to trace the growth of the stars born in the minihalos. In this section we describe the issues we still have to resolve as below, in order to reach the more accurate mass spectrum of the first stars. Interestingly, most of the ingredients we have not taken into consideration suggest that the mass of the first stars are overestimated to some extent in the present simulations. Hence, we would speculate the mass spectrum will shift to low mass side if we include all the missing effects into the simulations.

Resolution issues

In the present numerical experiment, we still do not have enough resolution. We set the sink radius r_{sink} to be 30AU, but the previous higher resolution studies of $r_{\text{sink}} \lesssim 1\text{AU}$ (but short time integration) revealed that the disk within 30AU also fragments into secondary stars (e.g. Clark et al. 2011a; Greif et al. 2012). They also found some of the fragments fall onto the primary, but the others are kicked to higher orbits to survive longer time. It is not certain that these stars survive without merging until the age of the system. However, we find low mass stars in our simulation similar to these stars,

that survive 10^5 yrs. Thus, we can speculate that our mass spectrum seems to underestimate the number of star at low mass side.

In addition, the simple mass accretion procedure onto the sinks employed in this experiment also introduce an overestimation of the mass of stars. In the present treatment the sinks are regarded as “black holes”, i.e. the vicinity of the sinks are “vacuum”. Thus the sink particles do not push the surrounding neighbor SPH particles. As a result, the mass accretion rate onto the sink particles are overestimated to some extent.

We also point out that the present resolution is not enough to capture the propagation of ionization front. In the SPH simulations, SPH particles are accumulated on the dense accretion disk and thereby very few particles reside in the polar less dense regions. As a result, the gas density at the SPH particles in the vicinity of the source star is always comparable to the density of the disk, which is larger than 10^7cm^{-3} . As was discussed in Susa (2013), the Strömgren radius of the protostar at this density is smaller than the SPH particle size (see Fig.9 of Susa (2013)). Thus, the fully ionized region does not emerge, i.e. hot ionized region of $> 2 \times 10^4 \text{K}$ does not form even in the vicinity of the massive protostars. Consequently, the ionization front do not break out by 10^5yr ¹⁰. However, in the present calculations, the H_2 photodissociation leads to the heating of gas via chemical H_2 formation heating. As was discussed in Susa (2013), H_2 formation heating becomes important in the presence of photodissociative radiation, since the photodissociation process is not a cooling process unlike the collisional dissociation processes. In other words, after an H_2 molecule releases its latent heat during its formation, photodissociation “pumps up” the H_2 molecule to a higher energy state (i.e. dissociated state) providing the energy by the radiation. Thus, strong radiative feedback exists in the present simulations even if the photoionization feedback does not come into play. Thus, if the effects of photoionization are taken into consideration properly, the radiative feedback effect will be enhanced.

We also mention another unknown factor related to the resolution. In this calculation, the structure of the disk inside the accretion radius is neglected. In fact we should have accretion disks inside the accretion radius if we have sufficient resolution. If the disk height inside the sink radius is not too high to shield the radiation penetrating into the outer region of the disk ($r > r_{\text{sink}}$), the present treatment is justified. However, if the shielding by the inner disk region is significant, our simulations overestimate the feedback effect. This is the unknown factor that might reduce the effects of radiation and increase the mass of the stars in our simulation, although it is not possible to infer the answer at present. These resolution issues will be investigated in the future.

HD cooling

¹⁰ The grid simulation can handle the polar low density regions more easily (Hosokawa et al. 2011), since the spatial resolution in such low density region is same as that in the dense disk. Lagrangian schemes like SPH change the resolution depending on the density. They have better resolution in the dense regions, but suffer low spatial resolution in less dense regions.

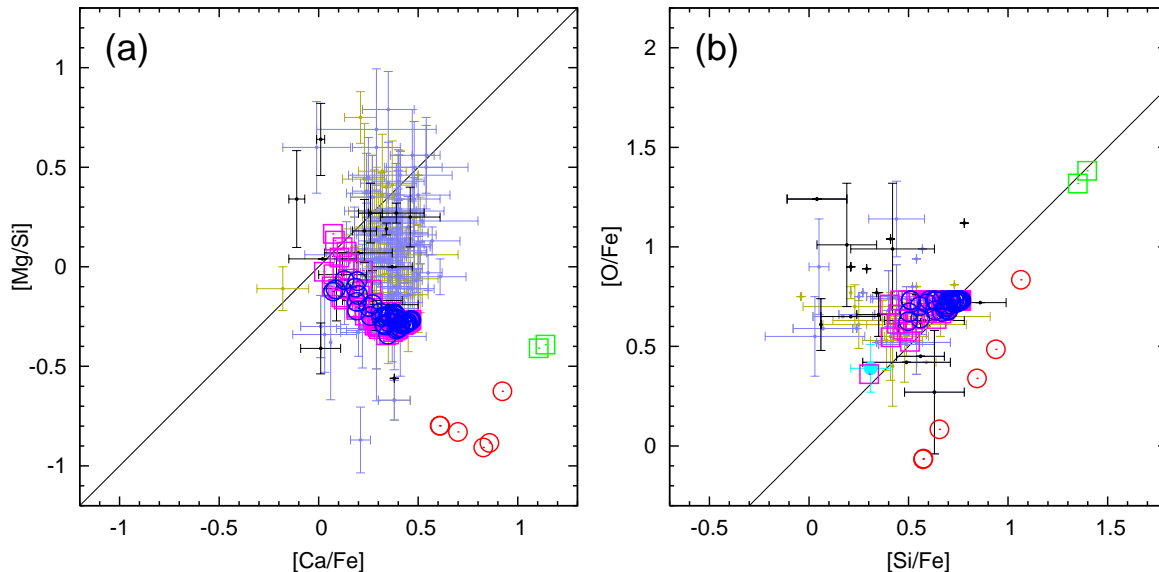
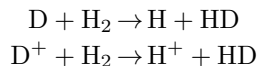


FIG. 21.— Abundance ratios, (a) $[\text{Mg}/\text{Si}]$ and $[\text{Ca}/\text{Fe}]$ and (b) $[\text{O}/\text{Fe}]$ and $[\text{Si}/\text{Fe}]$, of the yields of individual minihalos enriched by PISNe (*red*: Model IMF1 and *green*: Model IMF2) and CCSNe and AGB stars (*blue*: Model IMF1 and *magenta*: Model IMF2) and the metal-poor stars with $[\text{Fe}/\text{H}] < -3$ (*black*), $-3 < [\text{Fe}/\text{H}] < -2.5$ (*light blue*), and $-2.5 < [\text{Fe}/\text{H}] < -2$ (*yellow*) (Suda et al. 2011) and the average of the DLA systems (*cyan*: (Cooke et al. 2011)).

Importance of HD molecules has been discussed in the context of secondary population III stars, so called PopIII.2 stars. Since the excitation temperature is four times lower than that of the H_2 molecules, sufficient HD molecules cause additional cooling below $T \sim 100\text{K}$, which reduces the cloud mass/accretion rate, so does the mass of the stars. For the formation of HD molecules, abundant H_2 molecules are necessary, since the HD molecules mainly form via following reactions(Nakamura & Umemura 2002):



In addition, it is known that the HD molecules are favored at low temperatures(Yoshida et al. 2007; Solomon & Woolf 1973). Thus, the abundant H_2 at low temperature is crucial for HD cooling process, which is realized in the fossil HII regions after the death of other first stars or the shock heated gas in Ly- α cooling halos. Hirano et al. (2014) have shown that such condition could also be satisfied even in collapsing minihalos of $10^5 - 10^6 M_\odot$. In the present simulations we do not take into account the effects of HD cooling. Thus, the actual mass spectrum could be shifted to even lower mass when we include HD in our future calculations.

Radiative feedback from other sources

In the present cosmological simulations we do not include the effects of radiative feedback from other sources, since we concentrate on the formation of very first stars, i.e. the PopIII.1 stars. However, PopIII.2 stars also could contribute to the total star formation activities at the cosmic dawn, we should investigate the mass spectrum of such stars. As discussed above, the fossil HII regions could host less massive stars on average. We also point out that the radiative feedback by a nearby source also can reduce the mass of the stars(Susa et al. 2009). Hence the mass spectrum will be shifted to lower mass side.

The effects of LW background on the mass spectrum is still uncertain(e.g. Haiman et al. 1997; Machacek et al. 2001; Yoshida et al. 2003; Susa 2007), although it will reduce the star formation rate definitely.

The LW background intensity in unit of 10^{-21}cgs is as strong as 0.01 - 0.1 at $z \sim 10$ (e.g. Ahn et al. 2012), which could prevent the gas from cooling by destroying the H_2 molecules(Machacek et al. 2001; Yoshida et al. 2003; O'shea & Norman 2008). Suppression of H_2 cooling heats the gas, which makes the gas cloud gravitationally more stable. Thus, the LW background should hinder the formation of stars, because most of the minihalos ($\sim 90\%$) form at $8 \lesssim z \lesssim 20$ in our simulations. More massive halos of $\gtrsim 10^7 M_\odot$ could collapse due to the $\text{H}^- / \text{Ly}\alpha$ cooling even in the presence of strong LW radiation field(e.g. Omukai et al. 2008). In such conditions, high temperature might lead to the formation of more massive stars / massive black holes. Hence, the mass spectrum can potentially shifted to higher mass side if we include the contribution from PopIII.2 stars.

Streaming motion

Streaming motion is the relative motion of the baryon to the dark matter at small scale(Tselikhovich & Hirata 2010). It is typically 10km s^{-1} , which is larger than the escape velocity of the minihalos that host first stars. Thus, the minihalos that is not located at the bottom of the gravitational potential of larger scales cannot collapse to form stars in the presence of streaming motions. Consequently, the formation rate of the first stars will decrease significantly(Naoz et al. 2012). On the other hand, we do not find strong correlation between the mass spectrum and the properties of host dark matter halos such as the formation redshifts, the spin parameters and the halo mass (section4.6), which should have correlation with the position of the minihalos in larger scale. Thus, the mass spectrum might not be

affected by the streaming motion. In any case, we will explore this issue in a forthcoming paper.

Magnetic field

Recently, interests in the effect of magnetic fields on the first star formation is growing. The primordial gas is strongly coupled with the magnetic field during its contraction, and the field does not dissipate from the gas at the Jeans scale (Maki & Susa 2004, 2007), unlike in the local interstellar gas (e.g. Nakano & Umebayashi 1986). Thus, the magnetic field will be amplified more efficiently than the local counterpart. If the star forming gas cloud is magnetized with aligned field lines of sufficient strength, magnetic breaking and jet can transfer the angular momentum efficiently (Machida et al. 2008), and a single star forms without the accretion disk (Machida & Doi 2013). In addition, weaker field strength also affects the multiplicity of the stars (Machida & Doi 2013). However, the initial field strength, which can affect the dynamics of the star formation, is larger than the expected seed field strength in cosmological context (e.g. Gnedin et al. 2000; Turner & Widrow 1988; Ichiki et al. 2006; Xu et al. 2008; Ando et al. 2010; Doi & Susa 2011; Shiromoto et al. 2014). Thus, the magnetic field seemingly does not affect the first star formation.

On the other hand, it has been suggested that the magnetic field will be amplified very efficiently by turbulent motion in the minihalo (e.g. Schleicher et al. 2010; Schober et al. 2012). If this mechanism works and the amplified small scale field inversely cascades to larger scales smoothly, the host cloud of the first star could be magnetized enough. However, the sufficient amplification to affect the dynamics of the gas has not been shown starting from a very weak seed field of $\sim 10^{-18} - 10^{-20}$ G by *ab initio* numerical simulations so far (Sur et al. 2010; Federrath et al. 2011; Turk et al. 2012; Latif et al. 2013). Thus, the further progress on this issue is desired.

5.2. *Observational signatures of the mass spectrum*

The very massive first stars are luminous, but too far to be observed directly even by next generation huge telescopes¹¹. One of the most straight-forward way to observe the trace of the first stars is to investigate the abundance patterns of the low metallicity systems like EMP stars. As was discussed in section 4.7, the abundance patterns of PISNe are quite different from that of CCSNe. If the EMP stars are born from the unmixed remnants of the first stars, we might be able to find the clear evidence of the existence of PISNe. On the other hand, we have not found the PISNe so far. Thus, the mass spectrum to produce many PISNe (like IMF1) seems unlikely to represent the reality. Alternatively, if we find any evidence of PISNe in EMP stars in the future, the frequency of the presence of such stars would give us the information on the fraction of very massive stars of $> 140M_{\odot}$. Thus, such observation would give some constraint on the high mass end of the mass spectrum.

Another possible observation to give information on

the mass spectrum of the first stars is the hunting for the low mass zero-metallicity stars. As was discussed in the text, recent advance in the first star formation theory predicts some amounts of low mass stars of $\lesssim 1M_{\odot}$, which can survive the entire history of the Universe and thereby could be found in the MilkyWay halo. The number of such stars per single minihalo is still uncertain as of now even by state of art numerical simulations. Therefore, the number of such stars found by huge survey of halo stars would give constraint on the low mass end of the mass spectrum. Even if it is not found, we will have a strong constraint.

6. SUMMARY

We perform cosmological hydrodynamics simulations with non-equilibrium primordial chemistry to obtain 59 minihalos that host first stars. The obtained minihalos are used as the initial conditions of local three dimensional radiation hydrodynamics simulations to investigate the formation of the first stars. We employ the sink particles in the simulations that make it possible to trace the mass growth of the stars over 10^5 yrs. We regard the sink particles as stars and we take into account the radiative feedback from these stars using a protostellar evolution model.

Then we sum up all the stars found in 59 minihalos to construct the mass spectrum of the first stars. This is the first attempt to derive the mass spectrum of the first stars by cosmological simulations taking into account the fragmentation of the disk and the radiative feedback by the protostar. As a result, the spectrum peaks at several $\times 10M_{\odot}$, while the very massive stars of $> 140M_{\odot}$ also exist, which are the progenitors of PISNe. We find 2/3 of the minihalos host multiple stellar systems whereas the the rest of them have single stars. We also find the fraction of the minihalos that contain binaries is $\sim 50\%$, and the mean separation of the binaries is $10 - 1000$ AU.

Although most of the stars are massive ($\gtrsim 10M_{\odot}$), but we find a few stars are around $1M_{\odot}$. These stars are kicked by the others through three body interactions to a distant less dense region, where the mass accretion rates are very small. Since the stars of $< 0.8M_{\odot}$ can survive through the entire history of the Universe and the number of these low mass stars could be enhanced if we perform higher resolution simulations, hunting for the low mass first stars in the local Universe will an important observational attempt.

We also investigated the chemical imprints of the mass spectrum of the first stars on the observed low metallicity systems. We find that the yield of the heavy elements that is obtained by integrating the mass spectrum is not consistent with that of the low metallicity DLA systems / EMP stars, because the fraction of PISNe is too large. If we modify the mass spectrum to be shifted by 0.2 dex to the lower mass side, it is consistent with the observed data, although we still have small number of PISNe. If we consider the case that the EMP star is born in the remnant of an individual minihalo, the chemical imprint of PISNe is more prominent, because most of them are born as single stars. Thus we might be able to find the pure abundance pattern of PISN on EMP stars if they really formed in the ancient Universe.

¹¹ Their supernova explosions could be detected with upcoming optical and near-infrared surveys (e.g., Tanaka et al. 2013).

We thank T. Hosokawa for providing the data of protostars and S. Hirano, K. Omukai and N. Yoshida for fruitful discussions and careful reading of the manuscript. We also thank the anonymous referee for his/her constructive comments. We also thank T. Takeda for his help on the instruction of the visualization software Zindaiji3. We thank the support by Ministry of Education, Science, Sports and Culture, Grant-in-Aid for Scientific Research (C)22540295 (HS), (S)23224004 (NT), for Young Scientists (B)24740114(KH). KH also thanks the support by

MEXT HPCI STRATEGIC PROGRAM. A part of the simulations were performed with the K computer at the RIKEN Advanced Institute for Computational Science through the HPCI System Research project (Project ID: hp120286, hp130026), with XC30 "ATERUI" at the Center for Computational Astrophysics, CfCA, of National Astronomical Observatory, and with XE6 at the Institute for information Management and Communication, Kyoto University.

REFERENCES

- Abel, T., Bryan, G. L., & Norman, M. L. 2002, *Science*, 295, 93
 Ahn, K., Iliev, I. T., Shapiro, P. R., et al. 2012, *ApJ*, 756, L16
 Ando, M., Doi, K., & Susa, H. 2010, *ApJ*, 716, 1566
 Bate, M. R., Bonnell, I. A., & Price, N. M. 1995, *MNRAS*, 277, 362
 Bate, M. R., & Burkert, A. 1997, *MNRAS*, 288, 1060
 Beers, T. C., & Christlieb, N. 2005, *ARA&A*, 43, 531
 Bromm, V., Coppi, P. S., & Larson, R. B. 2002, *ApJ*, 564, 23
 Cayrel, R. et al. 2004, *A&A*, 416, 1117
 Chiaki, G., Yoshida, N., & Kitayama, T. 2013, *ApJ*, 762, 50
 Clark, P. C., Glover, S. C. O., & Klessen, R. S. 2008, *ApJ*, 672, 757
 Clark, P. C., Glover, S. C. O., Smith, R. J., et al. 2011, *Science*, 331, 1040
 Clark, P. C., Glover, S. C. O., Klessen, R. S., & Bromm, V. 2011, *ApJ*, 727, 110
 Coc, A., Uzan, J.-P., & Vangioni, E. 2013, *ArXiv e-prints*, 1307.6955
 Cooke, R., Pettini, M., Steidel, C. C., Rudie, G. C., & Nissen, P. E. 2011, *MNRAS*, 417, 1534
 Cooke, R., Pettini, M., Jorgenson, R. A., Murphy, M. T., Rudie, G. C., & Steidel, C. C. 2013, *MNRAS*, 431, 1625
 Croce, M., Pueblas, S., Scoccimarro, R. 2006, *MNRAS*, 373, 369
 Dhanoa, H., Mackey, J., & Yates, J. 2014, *arXiv:1402.1103*
 Doi, K., & Susa, H. 2011, *ApJ*, 741, 93
 Federrath, C., Sur, S., Schleicher, D. R. G., Banerjee, R., & Klessen, R. S. 2011, *ApJ*, 731, 62
 Fuller, T. M., & Couchman, H. M. P. 2000, *ApJ*, 544, 6
 Gnedin, N.Y., Ferrara, A., Zweibel, E.G. 2000, *ApJ*, 539, 505
 Greif, T. H., Johnson, J. L., Bromm, V., & Klessen, R. S. 2007, *ApJ*, 670, 1
 Greif, T. H., Springel, V., White, S. D. M., et al. 2011, *ApJ*, 737, 75
 Greif, T. H., Bromm, V., Clark, P. C., et al. 2012, *MNRAS*, 424, 399
 Haiman, Z., Thoul, A. A., & Loeb, A. 1996, *ApJ*, 464, 523
 Haiman, Z., Rees, M. J., & Loeb, A. 1997, *ApJ*, 476, 458
 Hasegawa, K., & Umemura, M. 2010, *MNRAS*, 407, 2632
 Hasegawa, K., Umemura, M., & Susa, H. 2009, *MNRAS*, 395, 1280
 Hasegawa, K., & Semelin, B. 2013, *MNRAS*, 428, 154
 Heger, A., & Woosley, S.E. 2002, *ApJ*, 567, 532
 Heger, A., & Woosley, S. E. 2010, *ApJ*, 724, 341
 Hirano, S., Hosokawa, T., Yoshida, N., et al. 2014, *ApJ*, 781, 60
 Hosokawa, T., & Omukai, K. 2009, *ApJ*, 691, 823
 Hosokawa, T., Omukai, K., Yoshida, N., & Yorke, H. W. 2011, *Science*, 334, 1250
 Hosokawa, T., Omukai, K., & Yorke, H. W. 2012, *ApJ*, 756, 93
 Ichiki, K., Takahashi, K., Ohno, H., Hanayama, H., Sugiyama, N. 2006, *Sci*, 311, 8271
 Jarosik, B. C. L. et al. 2011, *ApJS*, 192, 14
 Kitayama, T., & Yoshida, N. 2005, *ApJ*, 630, 675
 Kobayashi, C., Tominaga, N., & Nomoto, K. 2011, *ApJ*, 730, L14
 Komatsu, E. et al. 2011, *ApJS*, 192, 18
 Latif, M. A., Schleicher, D. R. G., Schmidt, W., & Niemeyer, J. 2013, *ApJ*, 772, L3
 Machacek, M. E., Bryan, G. L., & Abel, T. 2001, *ApJ*, 548, 509
 Machida, M. N., Matsumoto, T., & Inutsuka, S.-i. 2008, *ApJ*, 685, 690
 Machida, M. N., & Doi, K. 2013, *MNRAS*, 435, 3283
 Maki, H., Susa, H. 2004, *ApJ*, 609, 467
 Maki, H., Susa, H. 2007, *PASJ*, 59, 787
 Martel, H., Evans, N. J., II, & Shapiro, P. R. 2006, *ApJS*, 163, 122
 Naoz, S., Yoshida, N., & Gnedin, N. Y. 2012, *ApJ*, 747, 128
 Nakamura, F., & Umemura, M. 2002, *ApJ*, 569, 549
 Nakano, T., & Umebayashi, T. 1986, *MNRAS*, 218, 663
 Nishi, R., & Susa, H. 1999, *ApJ*, 523, L103
 Nomoto, K., Kobayashi, C., & Tominaga, N. 2013, *ARA&A*, 51, 457
 Omukai, K., Schneider, R., & Haiman, Z. 2008, *ApJ*, 686, 801
 Omukai, K., & Nishi, R. 1998, *ApJ*, 508, 141
 Omukai, K., & Palla, F. 2001, *ApJ*, 561, L55
 Omukai, K., & Palla, F. 2003, *ApJ*, 589, 677
 O'shea, B. W., & Norman, M. L. 2007, *ApJ*, 654, 66
 O'shea, B. W., & Norman, M. L. 2008, *ApJ*, 673, 14
 Pettini, M., King, D. L., Smith, L. J., & Hunstead, R. W. 1997, *ApJ*, 478, 536
 Ripamonti, E., & Abel, T. 2004, *MNRAS*, 348, 1019
 Sakuma, M., & Susa, H. 2009, *ApJ*, 698, 155
 Schleicher, D. R. G., Banerjee, R., Sur, S., Arshakian, T. G., Klessen, R. S., Beck, R., & Spaans, M. 2010, *arXiv:1003.1135*
 Schober, J., Schleicher, D., Federrath, C., et al. 2012, *ApJ*, 754, 99
 Shiromoto, Y., Susa, H., & Hosokawa, T. 2014, *ApJ*, 782, 108
 Smith, R. J., Glover, S. C. O., Clark, P. C., Greif, T., & Klessen, R. S. 2011, *MNRAS*, 414, 3633
 Spite et al. 2005, *A&A*, 430, 655
 Stacy, A., Bromm, V., & Loeb, A. 2011, *MNRAS*, 413, 543
 Stacy, A., Greif, T. H., & Bromm, V. 2012, *MNRAS*, 422, 290
 Stacy, A., & Bromm, V. 2013, *MNRAS*, 433, 1094
 Stacy, A., & Bromm, V. 2014, *ApJ*, 785, 73
 Stahler, S. W., Palla, F., & Salpeter, E. E. 1986, *ApJ*, 302, 590
 Stancil, P. C. 1994, *ApJ*, 430, 360
 Steinmetz, M., & Bartelmann, M. 1995, *MNRAS*, 272, 570
 Suda, T., Yamada, S., Katsuta, Y., Komiya, Y., Ishizuka, C., Aoki, W., & Fujimoto, M. Y. 2011, *MNRAS*, 412, 843
 Sur, S., Schleicher, D. R. G., Banerjee, R., Federrath, C., & Klessen, R. S. 2010, *ApJ*, 721, L134
 Susa, H., & Umemura, M. 2006, *ApJ*, 645, L93
 Susa, H. 2006, *PASJ*, 58, 445
 Susa, H. 2007, *ApJ*, 659, 908
 Susa, H., Umemura, M., & Hasegawa, K. 2009, *ApJ*, 702, 480
 Susa, H. 2013, *ApJ*, 773, 185
 Susa, H., & Umemura, M. 2004, *ApJ*, 600, 1
 Solomon, P. M., & Woolf, N. J. 1973, *ApJ*, 180, L89
 Tan, J. C., & McKee, C. F. 2004, *ApJ*, 603, 383
 Tanaka, M., Moriya, T. J., & Yoshida, N. 2013, *MNRAS*, 435, 2483
 Tegmark, M., Silk, J., Rees, M. J., et al. 1997, *ApJ*, 474, 1
 Tominaga, N., Umeda, H., & Nomoto, K. 2007b, *ApJ*, 660, 516
 Tominaga, N. 2009, *ApJ*, 690, 526
 Tominaga, N., Iwamoto, N., & Nomoto, K. 2013, *ArXiv e-prints*, 1309.6734
 Tseliakhovich, D., & Hirata, C. 2010, *Phys. Rev. D*, 82, 083520
 Turk, M. J., Abel, T., & O'Shea, B. 2009, *Science*, 325, 601
 Turk, M. J., Norman, M. L., & Abel, T. 2010, *ApJ*, 725, L140
 Turk, M. J., Oishi, J. S., Abel, T., & Bryan, G. L. 2012, *ApJ*, 745, 154
 Turner, M.S., Widrow, L.M. 1988, *Phys. Rev.D*, 37, 2743
 Umeda, H., & Nomoto, K. 2002, *ApJ*, 565, 385
 Umemura, M., Susa, H., Hasegawa, K., Suwa, T., & Semelin, B. 2012, *Prog. Theor. Exp. Phys.*, 01A306
 Whalen, D., van Veelen, B., O'Shea, B. W., & Norman, M. L. 2008, *ApJ*, 682, 49

- Wolcott-Green, J., Haiman, Z., & Bryan, G. L. 2011, MNRAS, 418, 838
- Xu, H., O'Shea, B., Collins, D., Norman, M., Li, H., & Li, S. 2008, ApJ, 688, L57
- Yong, D. et al. 2013, ApJ, 762, 26
- Yoshida, N., Abel, T., Hernquist, L. & Sugiyama, N., 2003, ApJ, 592, 645
- Yoshida, N., Omukai, K., Hernquist, L., & Abel, T. 2006, ApJ, 652, 6
- Yoshida, N., Oh, S. P., Kitayama, T., & Hernquist, L. 2007, ApJ, 663, 687
- Yoshida, N., Omukai, K., & Hernquist, L. 2008, Science, 321, 669